

Graphene-based Supercapacitors for Energy Storage

Applications

THESIS

Presented in Partial Fulfillment of the Requirements for the Degree Master of Science in
the Graduate School of The Ohio State University

By

Hao Yang

Graduate Program in Electrical and Computer Science

The Ohio State University

August 2013

Master's Examination Committee:

Professor Wu Lu, Advisor,

Professor Marvin H. White,

Professor Siddharth Rajan

Copyright by

Hao Yang

2013

Abstract

Although great efforts have been made on development of high performance Li-ion batteries and fuel cells in the past, the slow power capability and high maintenance cost have kept them away from many applications. Recently, supercapacitors have drawn great attention because of their high charge/discharge rate, long life cycle, outstanding power density and no short circuit concern. However, supercapacitors generally exhibit low energy density. The objective of this thesis research is to develop graphene-based supercapacitors with simultaneously high power density and energy density at low production cost. Supercapacitors, also known as ultracapacitors or electrochemical capacitors, store energy as electrical charge on highly porous materials. Currently one major challenge that keeps supercapacitors from their promising applications is their low energy density. One promising electrode material candidate for electric double-layer (EDL) supercapacitors is graphene. Graphene, due to its unique lattice structure, exhibits appealing electrical properties, chemical stability and high surface area. Ideally a monolayer of sp^2 bonded carbon atoms can reach a specific capacitance up to ~ 550 F/g as well as a high surface area of 2675 m^2/g . So far, a variety of methods have been developed to synthesis graphene starting from graphite, but the cost, graphene quality and productivity remain main obstacles for their industrial application. The porous graphene

material reported in this thesis was synthesized by a scalable oxidation-reduction method involving a rapid annealing process. The scanning electron microscopy (SEM) and transmission electron microscopy (TEM) images revealed the morphology and successful exfoliation of reduced graphene oxide (rGO). The interlayer distance characterized by X-ray diffraction (XRD) is 3.64 Å (24.44°) suggesting the removal of oxygen-containing functional groups, such as carbonyl, hydroxyl and carboxyl groups. In the X-ray photoelectron spectroscopy (XPS), the C/O ratio increases from ~2 to ~5 with O1s peak reduced significantly from graphite oxide (GO) to reduced graphene oxide. Furthermore, the successful reduction was verified by the low intensities of oxygen-related peaks in Fourier transform infrared spectroscopy (FTIR). In addition, the high Brunauer-Emmett-Teller (BET) specific surface area of 410 m²/g and mesoporous structure of the synthesized material would be beneficial to the improvement of charge-storage capability and thus energy density in supercapacitors. To evaluate the electrochemical performance of graphene electrodes, supercapacitors were assembled in symmetrical cell geometry. The near rectangular cyclic voltammetry (CV) curves with EMIMBF₄ and LiPF₆ at scan rate of 100mV/s suggest very efficient charge transfer within the porous graphene electrodes. The triangle charge-discharge responses with a small voltage drop and vertical spike in the low frequency region of a Nyquist plot indicates an ideal capacitor performance. The specific capacitance of 306.03 F/g and energy density of 148.75 Wh/kg at 1A/g were realized with highly porous graphene electrodes. Meanwhile, the power density extracted at 8A/g reaches ~10 kW/kg, thus, making it suitable for high power applications. Compared with previously investigated carbon-based EDL capacitors, the

supercapacitor based on the annealed graphene electrode is a milestone in terms of capacitance and energy density. Moreover, the supercapacitors assembled with graphene electrodes shows excellent stability for 10,000 charge-discharge cycles.

Dedicated with much love and affection to my beloved family,
my mentors and all of my friends.

Acknowledgments

Here, I would like to convey my deepest appreciation to my advisor, Dr. Wu Lu, for his expertise, patience and understanding throughout the whole period of my Master study at The Ohio State University. Without his guidance and encouragement, I would not have been able to complete this research and the thesis. It is my honor to have the chance to learn from him.

I would also like to express my sincerest gratitude to the other members of my committee, Dr. Marvin H. White and Dr. Siddharth Rajan, for their encouragement, thoughtful criticism, and assistance offered during my defense.

Special acknowledgement goes to Dr. Kannappan Santhakumar for his assistance in experiments and measurements during my research work in Gwangju Institute of Science and Technology (GIST), Gwangju, South Korea.

During this work, I got generous help from many lovely and warmhearted people. I am grateful to Dr. Jae-Hyung Jang for supporting my research in GIST, to Dr. Won Bae Kim, Dr. Jong Guk Kim, Dr. Yun Sung Lee, and Dr. S. Amaresh for the help in electrode preparation and supercapacitor cell assembly, and to Ms. So Hyun Choi, Ms. Ryu Ji Na and Ms. Park Min Joo for the registration work in GIST.

In addition, I appreciate the funding support from The Ohio State University and the World Class University (WCU) program of the Ministry of Education, Science and Technology (MEST) of Korea (Project No. R31-10026).

Many friends have offered their support and friendship which helped me maintain an optimistic attitude toward life and stay focused on my graduate study. I am grateful to Mr. Craig Gladwell and Mrs. Mary Beth Gladwell who helped me to get used to a new nation.

Most importantly, I wish to thank my parents and Ms. Rongqing Zhao for their love and encouragement throughout my master study.

Vita

2007-2011 B.S. Physics, Southeast University, Nanjing,
P. R. China

2011 to 2013 M.S. Electrical and Computer Engineering,
The Ohio State University, Columbus, OH,
USA

Fields of Study

Major Field: Electrical and Computer Engineering

Table of Contents

Abstract	ii
Acknowledgments	vi
Vita	viii
Fields of Study	viii
Table of Contents	ix
List of Tables.....	xii
List of Figures	xiii
Chapter 1 Introduction to Energy Storage Devices	1
1.1 Capacitors	2
1.2 Batteries	5
1.3 Fuel cells.....	7
1.4 Supercapacitors	9
1.5 Comparison of Energy Storage Devices.....	11
1.6 Research Motivations and Objectives	14
1.7 Organization of Thesis	15

Chapter 2 Graphene-based Supercapacitor	16
2.1 Types of Supercapacitors.....	17
2.2 Electrode Materials	18
2.2.1 Electric double layer capacitance	18
2.2.2 Pseudocapacitance	30
2.2 Electrolytes	32
2.3 Separators	34
2.4 Summary.....	34
Chapter 3 Synthesis of Graphene and Material Characterization Results	36
3.1 Synthesis Process	37
3.1.1 Preparation of graphene oxide (GO).....	37
3.1.2 Preparation of reduced graphene oxide (rGO)	38
3.2 Material Characterization	39
3.2.1 Scanning electron microscopy.....	39
3.2.2 Transmission electron microscopy	40
3.2.3 Nitrogen isothermal adsorption measurement.....	41
3.2.3 X-ray diffraction	43
3.2.3 Raman spectrum	44

3.2.3 X-ray photoelectron spectra	45
3.2.3 Fourier transform infrared spectrum.....	46
3.3 Conclusion	47
Chapter 4 Supercapacitor Assembly and Electrochemical Measurements.....	49
4.1 Supercapacitor assembly	49
4.2 Electrochemical performance of the graphene electrodes.....	50
4.2.1 Cyclic Voltammetry.....	50
4.2.2 Galvanostatic charge-discharge	51
4.2.3 Electrochemical impedance spectroscopy.....	54
4.2.4 Energy density and power density	55
4.3 Conclusion	57
Chapter 5 Conclusions and Future Work.....	59
References	61
Appendix A: List of abbreviations	72

List of Tables

Table 1.1 Comparison of capacitors, batteries, fuel cells and supercapacitors [11-20]. ...	13
Table 2.1 Comparison of different carbon materials for supercapacitors [66].	29
Table 4.1 Performance comparison of reported graphene-based supercapacitors	57

List of Figures

Figure 1.1 Schematic of an electrostatic capacitor.....	3
Figure 1.2 Schematic of a Li-ion battery.	7
Figure 1.3 Schematic of a proton exchange membrane fuel cell [13].	8
Figure 1.4 Schematic of a supercapacitor.	10
Figure 1.5 Ragone plot for various energy storage devices [14].	11
Figure 2.1 Classification of supercapacitors and related electrode materials [8].....	18
Figure 2.2 Models of electric double layer at positively charged surface: (a) the Helmholtz model, (b) the Gouy-Chapman model, (c) the Stern model [30].	19
Figure 2.3 Three-dimension view of ideal graphene crystalline structure.	26
Figure 3.1 Schematic of synthesis process.	36
Figure 3.2 (a) and (b) are scanning electron microscopy images at low and high magnification, (c) and (d) are field emission scanning electron microscopy images of HAG sample.....	39
Figure 3.3 Transmission electron microscopy images of HAG sample.	40
Figure 3.4 (a) Nitrogen adsorption/desorption analysis of HAG sample, (b) Pore size distribution versus the pore width.	41
Figure 3.5 X-ray diffraction patterns of GO and HAG.	43
Figure 3.6 Raman spectrum of HAG.	44

Figure 3.7 X-ray photoelectron spectra of GO and HAG.....	45
Figure 3.8 Fourier transform infrared spectrum of HAG.	47
Figure 4.1 Schematic of the symmetrical supercapacitor structure and image of the assembled device.	49
Figure 4.2 Cyclic voltammetry curves for HAG supercapacitors with (a) ionic liquid and (b) LiPF_6 electrolyte at different scan rates.	50
Figure 4.3 galvanostatic charge-discharge curves of HAG supercapacitors with (a) ionic liquid and (b) LiPF_6 electrolyte at different current densities.....	51
Figure 4.4 Specific capacitances of HAG supercapacitors calculated from GCD curves at various current densities.	52
Figure 4.5 Cycling stability of the HAG supercapacitors after 10000 cycles.	53
Figure 4.6 Nyquist plot for HAG supercapacitors.	55
Figure 4.7 Ragone plot of the HAG supercapacitors.....	56

Chapter 1 Introduction to Energy Storage Devices

Due to climate change and fast development of the global economy, energy has become a primary focus in the scientific and industrial communities. With concerns of the environment pollution, increasing mining cost and the depletion of fossil fuel, there is an urgent need for an efficient, clean and renewable energy source, and energy storage technique [1].

Although great efforts have been made on the development of high performance Li-ion batteries and fuel cells [2-4], the poor power capability and high maintenance cost have kept them away from many applications. Recently, supercapacitors have drawn great attention because of their high charge discharge rate, long life cycle, outstanding power density and no short circuit concern that are of concern with current batteries or fuel cells. Supercapacitors, also known as ultracapacitors or electrochemical capacitors, store energy with an electric double layer (EDL) capacitance achieved by ion adsorption or pseudocapacitance dominated by surface redox reaction. Pseudocapacitors with conducting polymers or metal oxides as electrode material, although demonstrate a high capacitive performance, but cannot maintain this performance after prolonged cycling. On the other hand, EDL capacitors can be charged and discharged as many as one million

cycles without performance degradation [5]. Furthermore, ion transportation is faster than a redox reaction, resulting in a high charge-discharge rate and power density in EDL capacitors. Currently, the energy density of EDL capacitors is generally 3-5 Wh/kg, which is one order of magnitude below commercialized lithium-ion batteries (100-275 Wh/kg) [6, 7]. Thus, increasing the energy capacity with minimum sacrifice of power density is now a major topic in supercapacitor research.

Currently, the three major commercialized energy storage devices are capacitors, batteries and fuel cells. To illustrate the advantage of supercapacitors, the structure, mechanism and performance comparison of those devices are discussed in the following sections of this chapter.

1.1 Capacitors

A capacitor, which is a passive electrical device, stores energy as charge in the electrical field between two conducting plates called electrodes. Capacitors generally can release the stored charge quite fast resulting in a high power, but cannot store much energy.

Conventional capacitors, also known as electrostatic capacitors, consist of two conducting electrodes separated by an insulating layer called a dielectric, as shown in Figure 1.1. When applying an external voltage, charges accumulated on the surfaces of the two electrodes which are isolated by an insulating dielectric layer, thus, generating an electric field. The resulting electric field allows the device to store energy.

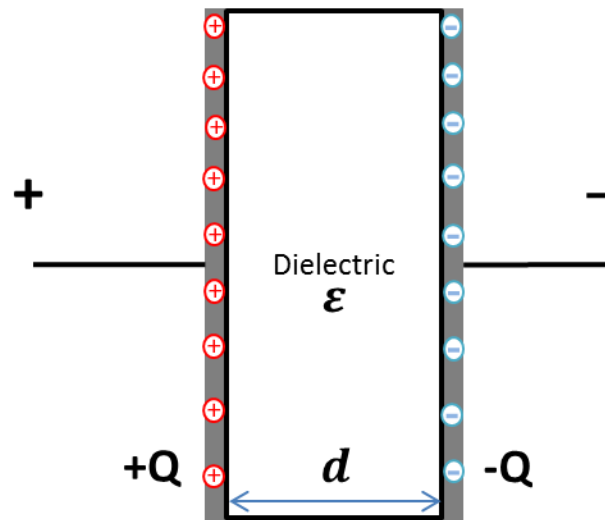


Figure 1.1 Schematic of an electrostatic capacitor.

The capacitor can be characterized by a parameter called the capacitance C , which is defined as the ratio of the charge Q to the applied voltage V :

$$C = \frac{Q}{V} \quad (1-1)$$

where the capacitance may vary with the applied voltage in some circumstances. In this case, the capacitance can be written as the derivative of charge with respect to the applied voltage:

$$C = \frac{dQ}{dV} \quad (1-2)$$

For a capacitor consisting of two parallel plates with surface area of A separated by a dielectric with permittivity of ϵ and a thickness of d , the voltage is defined as the integral of the electric field ξ with respect to the spacing:

$$V = - \int_0^d \xi dx = \iint_0^d \frac{\rho}{\epsilon} dx = \int_0^d \frac{Q}{\epsilon A} dx = \frac{Qd}{\epsilon A} \quad (1-3)$$

So, the capacitance can be extracted as:

$$C = \frac{\epsilon A}{d} \quad (1-4)$$

In order to achieve high capacitance, one needs to find dielectric materials with high permittivity, to shorten the distance between electrodes, and more importantly to discover novel electrode materials with highly developed surface area. As reported [8-11], potential candidates of the electrode material are carbon related materials with outstanding conductivity and porous structure, like activated carbon, carbon aerogel, carbon nanotube and graphene. The porous surface offers a high charge storage capability in a limit size of a packaged device.

For an energy storage device, two primary characteristics of the performance are energy density (or specific energy) and power density (or specific power). Those values are defined as the energy or power per unit mass. The energy E stored in a capacitor is:

$$E = \frac{1}{2} CV^2 = \frac{Q^2}{2C} \quad (1-5)$$

To determine power density P , the time ∂t required to discharge the capacitor is needed.

$$P = \frac{\partial E}{\partial t} \quad (1-6)$$

Generally, conventional capacitors have very high power density higher than 5000 W/kg, but low energy density in the range of 0.01-0.05 Wh/kg. Compared with batteries and fuel cells, capacitors can be charged or discharged rapidly, but cannot store a large amount of energy.

1.2 Batteries

So far, batteries have become the most common power source for various applications in industrial and consumer electronics. A battery is a device that converts stored chemical energy into electrical energy through a redox reaction. A typical battery contains one or more electrochemical cells. Each electrochemical cell consists of two electrodes which are electrically connected by a conductive electrolyte with anions (negative charge ions) and cations (positive charge ions). The polarity of a cell is identified by the transport of the anions and cations. In the charging process, the electrode with anions transport is called the anode or negative electrode, while the other electrode with cations transport is called the cathode or positive electrode. Generally, batteries are powered by a redox reaction with a reduction of cations at the cathode and an oxidation of anions at the anode.

Based on their charging capability, batteries can be divided into two types: disposable batteries and rechargeable batteries. Disposable batteries, for example the zinc-carbon batteries and alkaline batteries, are designed to irreversibly convert the

chemical energy into electric energy. On the other hand, the rechargeable batteries can restore the original composition with charging process (e.g. lead-acid, nickel metal hydride (NiMH), nickel-zinc (NiZn), nickel-cadmium (NiCd), and lithium-ion cells). As a consequence, disposable batteries have higher energy density than rechargeable batteries.

Currently lithium-ion batteries (Figure 1.2) represent the best electrochemical cells with a high energy density of 120-170 Wh/kg, moderate weight and no memory effect as well [11]. In spite of their high specific energy, the lithium-ion batteries and their substitutes are suffering from a low charge-discharge rates or low power density. Generally, the anode of a commercial lithium-ion cell is made of graphite or other carbon materials. Typically, the cathode material is lithium intercalated compounds like iron phosphate, cobalt oxide, manganese oxide, and nickel oxides. The lithium ions can migrate into and away from both electrodes. During the charging process, the lithium ions move into the graphite anode. In the discharge process, when connected to an external load, the ions migrate back to the cathode. The lithium ion is highly reactive and can react with water in the electrolyte forming hydrogen gas and lithium hydroxide. Thus, the organic electrolyte and a well-sealed packaging method are employed in lithium ion batteries to minimize the possibility of dangerous reactions.

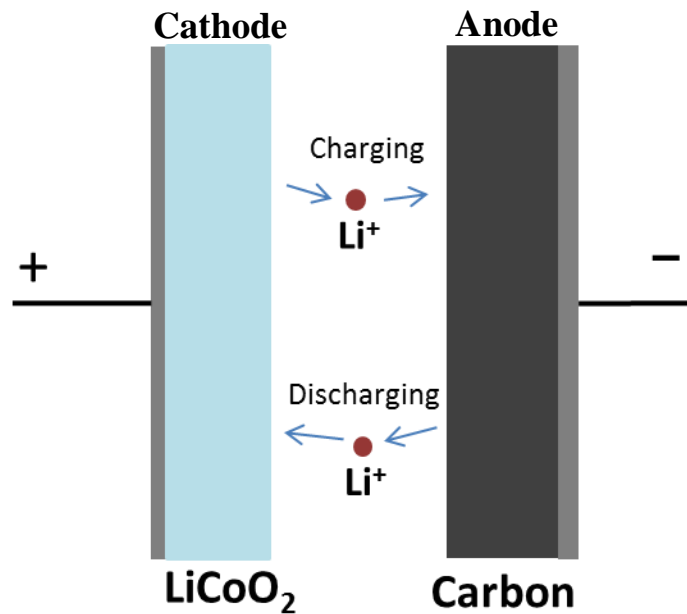


Figure 1.2 Schematic of a Li-ion battery.

1.3 Fuel cells

Similar to batteries, fuel cells convert the chemical energy of a fuel into electric energy, shown in Figure 1.3. However, fuel cells require no recharging and the byproduct of the reaction generally is environmentally friendly like water and heat. As long as the fuel supply is adequate and consistent, the cell can work ideally without replacement with outstanding reliability. Compared with thermomechanical methods, fuel cells do not have combustion as an intermediate step, which results in a higher energy conversion efficiency of 40%-60% [12]. For these reasons, fuel cell technology has become a clean, economical and reliable solution for power sources. Among all the commercialized energy storage alternatives, fuel cells hold one of the highest energy densities above 500

Wh/kg, although their low power density remains an obstacle for use in high power applications.

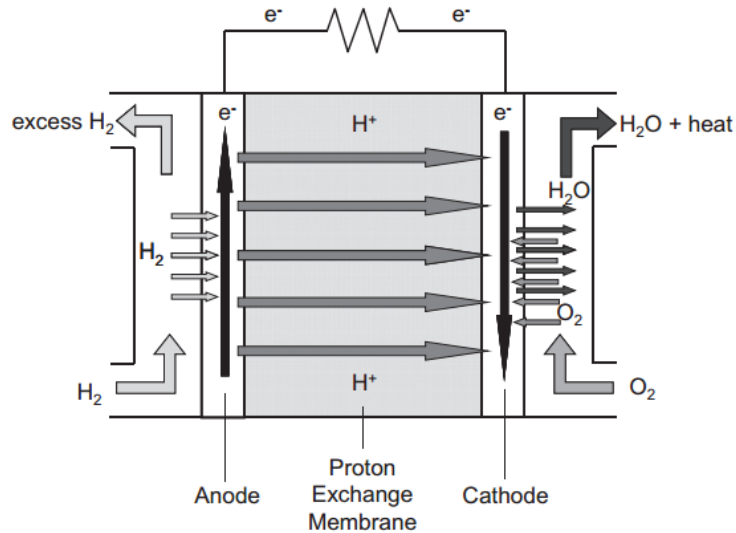


Figure 1.3 Schematic of a proton exchange membrane fuel cell [13].

Generally, a fuel cell consists of a cathode, an anode and an electrolyte in its construction. The major difference among various types of fuel cells is the electrolyte. Common electrolytes in both research and commercial devices are aqueous alkaline solution, polymer membrane and ceramic oxide. The most popular fuel cell design is the hydrogen proton exchange membrane (PEM) fuel cell. With hydrogen introduced to the anode, a catalyst oxidizes hydrogen turning them into protons (hydrogen ions) and electrons. The PEM is designed to allow positively charged ions to pass through to the other side, thus electrons accumulate on the anode side. When connecting with a load,

electrons will migrate along the external circuit to the cathode, and combine with protons from the anode under the presence of oxygen.

1.4 Supercapacitors

Because of slow power delivery of batteries and fuel cells and the urgent needs for high power energy storage systems, more and more attention has been given to supercapacitors. A typical schematic of supercapacitor is shown in Figure 1.4. Similar to the sandwiched structure of capacitors, supercapacitors are constructed from two highly porous electrodes. Those two electrodes are immersed into an electrolyte, and separated by a dielectric membrane which allows ions to pass through. When applying an external electric field to the device, positive and negative charges accumulate on surfaces of both electrodes. Because of the natural attraction law of opposite charges, ions in the electrolyte solution diffuse across the separator and get into the pores of the electrodes. And the electrodes are engineered to prevent the recombination of ions. Hence, a double layer of charges is formed at each electrode. To achieve higher energy density and capacitance, porous materials with larger surface area and thinner distance between electrodes are desired in supercapacitors' electrodes based on their energy storage mechanism.

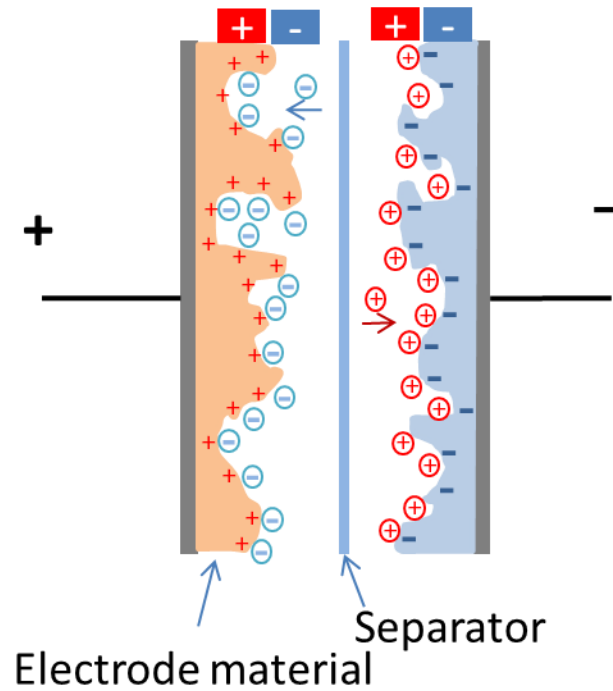


Figure 1.4 Schematic of a supercapacitor.

Governed by the same basic principles as capacitors, supercapacitors utilize electrodes with high surface area and thin membrane as a dielectric layer. As a result, the capacitance and energy would be improved dramatically. In addition, with a low equivalent series resistance (ESR) value that is comparable to conventional capacitors, they can maintain a very high power density. More detailed discussions of each component of supercapacitor will be given in Chapter 2.

1.5 Comparison of Energy Storage Devices

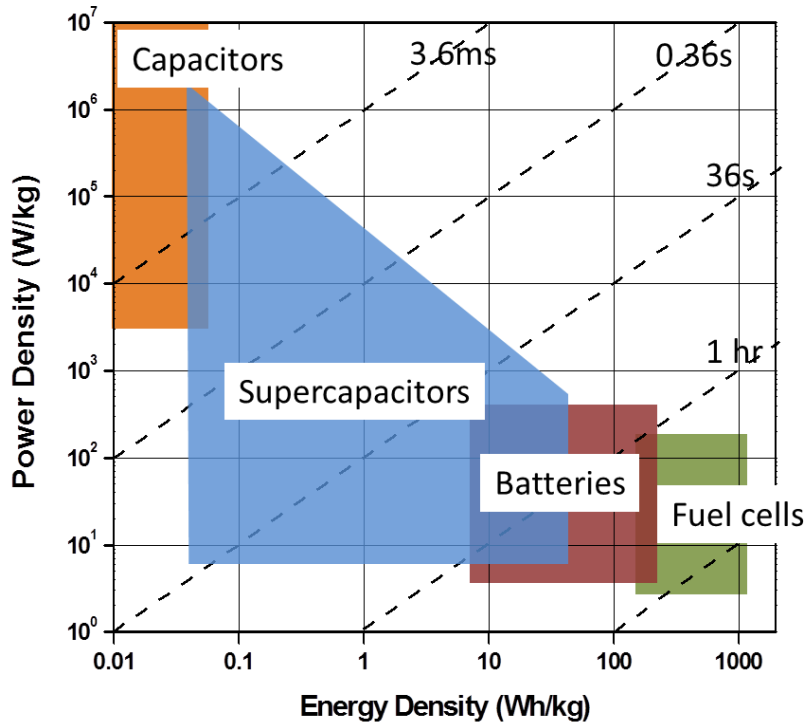


Figure 1.5 Ragone plot for various energy storage devices [14].

The Ragone chart (Figure 1.5) is a standard method to visualize the energy storage performance of various devices [14]. The dash lines indicate the time required to charge or discharge the device. From the chart, we can see that compared with batteries or fuel cells, conventional capacitors have very high power density, but relatively low energy density. It means that a conventional capacitor can be charged or discharged very quickly

and generate a high power, but it cannot storage much energy in unit mass or volume. On the other hand, batteries and fuel cells can storage more energy, but have a poor dynamic performance. Supercapacitors store more power than a battery and more energy than a capacitor. It means that supercapacitor can be charged or discharged very fast and maintain a reasonable energy stored per unit mass. For this reason, it brings significant benefits in peak-power delivery applications, like regenerative braking, electric vehicle acceleration and uninterruptible power supply.

Besides bridging the power gap between capacitors and batteries, supercapacitors also hold many other desirable properties that make them a promising candidate for the next generation energy storage device. The charge storing mechanism is a physical process without any chemical or phase change, so that it is highly reversible and can be repeated for a large number of charge-discharge cycles, up to 1 million times [15,16]. Also, they can be operated over a wide temperature range.

Table 1.1 reveals the detailed performance differences for those devices. Despite of the technical advantages like fast charge-discharge rate, longer cycle life, high power density, low weight and low toxicity, one critical obstacle of supercapacitors' application is the high cost. To achieve a higher performance, researchers are exploring new electrolyte that can improve the operating voltage range, novel dielectric layer with better porosity, thinner thickness and higher permittivity, and conducting material with larger surface area that requires simple or even one-step synthesis method. All of those improvements involve high cost processes or materials that push the systematical cost of supercapacitors to a value of 10-20 dollars per watt hour [18]. For comparison, the unit

cost for batteries is only 1-2 dollars per watt hour which is nearly one tenth of supercapacitors’.

Parameters	Capacitors	Batteries	Fuel cells	Supercapacitors
Charge/discharge time	1 ps-1 ms	1-10 hours	Not applicable	1 ms-1 s
Cycle life (cycles)	More than 1 million	150-2,000	Not applicable	Up to 1 million
Energy density (Wh/kg)	0.01-0.3	30-265	500-2,000	0.5-20
Power density (W/kg)	>5,000	100-3,000	1-1,000	5,000-10,000
Cost per Wh	0.10-1.00	1-2	0.035-0.05	10-20
Operating voltage range (V)	6-800	1.2-4.2	0.6-0.7	1.0-4.5
Operating temperature range (°C)	-20 to +100	-20 to +65	+50 to +1000	-40 to +85

Table 1.1 Comparison of capacitors, batteries, fuel cells and supercapacitors [11-20].

1.6 Research Motivations and Objectives

To overcome the major obstacles of supercapacitor research: the low energy density and high cost, improvement of current technologies are needed in the studies of scalable synthesis approach of graphene that provides better exfoliation and morphology at low cost, electrode preparation method which can retain the porous structure and electrical properties of active material, and the cell architecture for better electrochemical performance. To realize that goal, an effective synthesis routine of 2D material, a new electrolyte with high voltage tolerance and better cell assembly method to minimize the ESR value are critical aspects of the research.

The general purpose of the research is to enhance the performance of supercapacitors, to reduce the cost and to miniaturize the size. The performance enhancement can be characterized as parameters such as voltage limit, specific capacitance, energy density, power density and life time.

Herein, this thesis presents a one-step synthesis route of few-layered graphene sheets that achieves high EDL capacitance of 306.3 F/g at 1 A/g. This process is based on the reduction reaction of graphite oxide with the assistance of hydrogen gas at a relatively low temperature. Ionic liquid electrolyte can improve the operation voltage to 4V providing significant benefits for energy storage performance. In addition, the electrochemical measurement results of cell assembled in lithium salt electrolyte were given as comparison. Both of the high capacitance and the wider operating voltage contribute to the increasing of energy density to an exceptionally high value 148.75

Wh/kg at a current density of 1 A/g measured at room temperature. Meantime, the power density at 8 A/g reaches ~10k W/kg which makes it suitable for high power applications.

1.7 Organization of Thesis

The rest of this thesis is structured as the following.

In Chapter 2, each component of graphene-based supercapacitors will be discussed to illustrate their necessity, advantages and possible improvements. The components to be discussed are electrode material, electrolyte and separator.

In Chapter 3, material synthesis details and characterization results will be provided. Characterization involves multiple techniques like scanning electron microscopy (SEM), transmission electron microscopy (TEM), nitrogen isothermal adsorption, X-ray diffraction (XRD), Fourier transform infrared spectroscopy (FTIR), X-ray photoelectron spectroscopy (XPS) and Raman spectroscopy to reveal the reduction and exfoliation of graphene by the modified synthesis method.

Chapter 4 discusses the assembly and testing of supercapacitor cells using synthesized reduced graphene oxide with ionic liquid and lithium salt electrolyte. Electrochemical measurements are used to extract the specific capacitance, energy density and power density, and the Ragone plot will be compared to show the performance differences between electrolytes.

Chapter 5 summarizes the research work and results of this master thesis. Some future work to improve the performance will be suggested.

Chapter 2 Graphene-based Supercapacitor

To improve the energy density, a porous electrode material with highly developed surface area and high electric conductivity is desired. Carbon materials, due to their low cost, various microtexture and processability, are more attractive than other materials [8]. Activated carbons, carbon aerogels and carbon nanotubes have been widely researched before. Activated carbon materials are commonly used in EDL supercapacitors. The reported specific surface area of activated carbon ranges from 500 to 2000 m²/g [9, 10], but only a fraction of it can contribute to the capacitance. This is believed to be caused by the presence of inaccessible micropores (< 2 nm) for electrolyte [11], preventing those surface from storing charge leading to a low specific capacitance of 160 F/g in aqueous electrolyte and 100 F/g in organic electrolyte [21]. Carbon nanotubes have a moderate surface area as well as a good conductivity. Supercapacitors based on carbon nanotubes don't demonstrate good capacitive performance until a pseudocapacitive component is added [22], and the manufacturing difficulties plus cost further limit their possibility of implementation in actual devices.

This chapter will present the overview of electrodes, electrolyte, and dielectric of supercapacitors. It will help to understand the necessity of graphene-based

supercapacitors and how to enhance the electrochemical properties by altering the components. To start with, the types of supercapacitors will be discussed.

2.1 Types of Supercapacitors

According to the energy storing principles, supercapacitors can be divided into three types: electric double layer capacitors, pseudocapacitors and hybrid capacitors, as shown in Figure 2.1. EDL capacitors store electric energy electrostatically into Helmholtz double layer at the interface between electrode and electrolyte. The typical electrode materials for EDL capacitors are carbon-based, like activated carbon (AC), carbon aerogel, carbon nanotube (CNT) and newly introduced graphene. Pseudocapacitors, by contrast, achieve energy storage with redox reaction with the charge transfer between electrode and electrolyte. The typical electrode materials for pseudocapacitors are conducting polymers (e.g. polyaniline, polypyrrole, polythiophene and derivatives of polythiophene) [23] and metal oxides (e.g. ruthenium oxide, manganese oxide, tin oxide, cobalt oxide) [24-27]. But both EDL capacitors and pseudocapacitors are not perfect for practical applications due to the disadvantages like low capacitance in EDL capacitors and stability problem in pseudocapacitors. Thus, hybrid devices with composites of carbon material and pseudocapacitive additive were investigated to combine the two energy storage mechanisms [28, 29]. The devices can be easily distinguished from each other by the electrode material.

It is convenient to discuss the electrode materials in terms of EDL capacitance and pseudocapacitance separately.

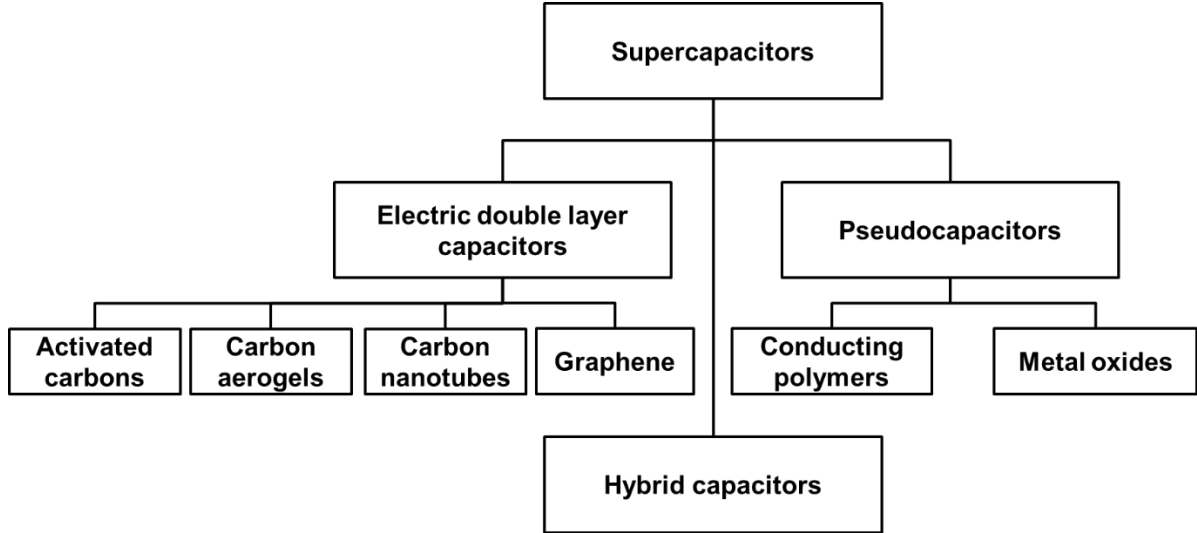


Figure 2.1 Classification of supercapacitors and related electrode materials [8].

2.2 Electrode Materials

2.2.1 Electric double layer capacitance

EDL capacitors utilize the electric double layer to storage charge, as described in section 1.4. Various models were developed to illustrate the EDL charge distribution, as shown in Figure 2.2 [30]. As a fact, polar aprotic solvents (e.g. acetonitrile) are good at solvating cations, but not anions, while polar protic solvents (e.g. water and alcohols) are much better at solvating anions. Since typical electrolyte solvents used in supercapacitors are polar protic solvents, so the cations are highly solvated but the anions are not. The earliest model was reported by von Helmholtz in the 19th century in his research

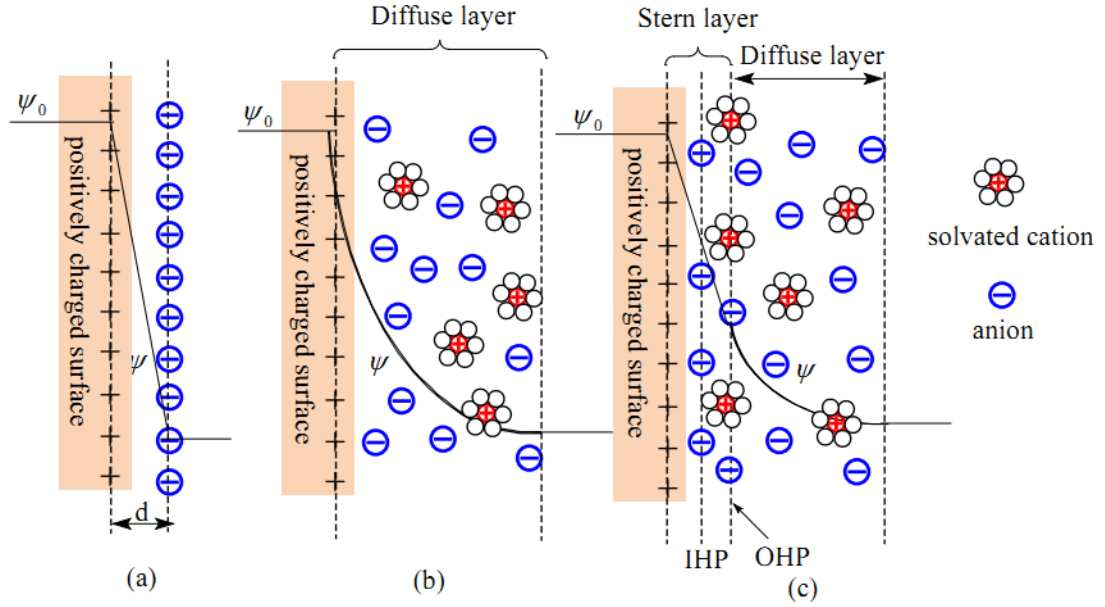


Figure 2.2 Models of electric double layer at positively charged surface: (a) the Helmholtz model, (b) the Gouy-Chapman model, (c) the Stern model [30].

regarding the distribution of opposite charges at the interface of colloidal particles [31]. The Helmholtz model treats the EDL as a simple capacitor that two layers of opposite charges form at the interface of electrode and electrolyte separated with a distance. So at the positively charged side, a layer of anions is adsorbed at the surface forming a linear electric potential profile. The capacitance of the Helmholtz layer is given by:

$$C_H = \frac{\epsilon}{d_H} \quad (2-1)$$

where d_H is the thickness of the Helmholtz layer and ϵ is the permittivity of the electrolyte solutions. The thickness d_H can be approximated as the radius of solvated ions.

Helmholtz model while providing the simplest approximation hypothesizes ideal layers of opposite charges which do not exist in nature. And it does not account for factors like diffusion of ions, the possibility of absorption on the surface and the interaction between solvent dipole moments and electrode.

In order to explain the continuous charge distribution (cations and anions in electrolyte) driven by thermal motion of ions, Luois Georges Gouy and David Chapman introduced the diffuse double layer model [32, 33]. It assumes that the concentration of the ions near a charged surface follows the Boltzmann distribution:

$$n = n_0 \exp\left(-\frac{ze\psi(x)}{k_B T}\right) \quad (2-2)$$

where n_0 is the bulk concentration of the ion, z is ionic valence, e is electron charge, ψ is the potential, k_B is Boltzmann constant, and T is the temperature. Thus, the charge density of the electrolyte can be written as:

$$\rho(x) = e \sum_i z_i n_{0i} \exp\left(-\frac{z_i e \psi(x)}{k_B T}\right) \quad (2-3)$$

For symmetrical electrolyte with $z_+ = -z_- = z$, $n_{0+} = n_{0-} = n_0(\infty)$, we have:

$$\rho(x) = -zen_0 \left(\exp\left(\frac{ze\psi(x)}{k_B T}\right) - \exp\left(-\frac{ze\psi(x)}{k_B T}\right) \right) \quad (2-4)$$

According to Poisson equation, for a planar surface:

$$\frac{d^2\psi}{dx^2} = -\frac{\rho}{\varepsilon} \quad (2-5)$$

where ε is the permittivity of the electrolyte solutions.

By combining the Boltzmann and Poisson equations, we can get:

$$\frac{d^2\psi(x)}{dx^2} = \frac{2zen_0}{\epsilon} \left[\frac{\exp\left(\frac{ze\psi(x)}{k_B T}\right) - \exp\left(-\frac{ze\psi(x)}{k_B T}\right)}{2} \right] \quad (2-6)$$

By introducing substitution:

$$y = \frac{ze\psi(x)}{k_B T}, \quad \lambda_D = \left[\frac{\epsilon k_B T}{2n_0 e^2 z^2} \right]^{1/2}$$

Equation 2-5 can be rewritten as:

$$\frac{d^2y}{dx^2} = \frac{1}{\lambda_D^2} \sinh(y) \quad (2-7)$$

Considering boundary conditions $y|_{x=\infty} = \frac{dy}{dx}|_{x=\infty} = 0$ and the identity $\frac{1}{2} \frac{d}{dx} \left(\frac{dy}{dx} \right)^2 =$

$\frac{dy}{dx} \frac{d^2y}{dx^2}$, we can obtain:

$$\frac{1}{2} \frac{d}{dx} \left(\frac{dy}{dx} \right)^2 = \frac{dy}{dx} \frac{1}{\lambda_D^2} \sinh(y) \quad (2-8)$$

After integration,

$$\frac{1}{2} \int_{\left(\frac{dy}{dx}\right)^2}^0 d \left(\frac{dy}{dx} \right)^2 = \int_y^0 \frac{1}{\lambda_D^2} \sinh(y) dy$$

$$\frac{dy}{dx} = -\frac{1}{\lambda_D} \sqrt{2(\cosh(y) - 1)} = -\frac{2}{\lambda_D} \sinh\left(\frac{y}{2}\right) \quad (2-9)$$

And after another integration with boundary condition $y|_{x=0} = y_0$,

$$\int_{y_0}^y \frac{1}{2\sinh\left(\frac{y}{2}\right)} dy = \int_0^x -\frac{1}{\lambda_D} dx$$

$$\ln\left(\frac{e^{y/2}-1}{e^{y/2}+1}\right) - \ln\left(\frac{e^{y_0/2}-1}{e^{y_0/2}+1}\right) = -\frac{x}{\lambda_D} \quad (2-10)$$

The solution of the above equation is [34]:

$$y = 2 \ln\left(\frac{e^{y_0/2}+1+(e^{y_0/2}-1)e^{-x/\lambda_D}}{e^{y_0/2}+1-(e^{y_0/2}-1)e^{-x/\lambda_D}}\right) \quad (2-11)$$

Therefore, the potential distribution is given by [35]:

$$\psi(x) = \frac{2k_B T}{ze} \ln\left(\frac{e^{\psi_0/2}+1+(e^{\psi_0/2}-1)e^{-x/\lambda_D}}{e^{\psi_0/2}+1-(e^{\psi_0/2}-1)e^{-x/\lambda_D}}\right) \quad (2-12)$$

where ψ_0 is the value of ψ at $x = 0$. The above equation is similar to a simple exponential equation. Therefore, the potential decreases exponentially from the metal surface to the electrolyte.

Then, the capacitance of the diffusion layer can be written as:

$$C_{diff} = \frac{Q_{diff}}{\psi_0} = \frac{-\varepsilon k_B T d\psi/dx}{ze\psi_0} = \frac{2\varepsilon k_B T}{ez\lambda_D \psi_0} \sinh\left(\frac{ze\psi_0}{2k_B T}\right) \quad (2-13)$$

If $\psi \ll 2k_B T/ze$ is satisfied, the capacitance is approximated as:

$$C_{diff} = \frac{\varepsilon}{\lambda_D} \quad (2-14)$$

The Gouy-Chapman model overestimates the EDL capacitance. It assumes that ions act like point charges and there is no physical limitation for ions' approach to the surface, which is not true [30]. The capacitance of two separated arrays of charges is inversely proportional to the separation distance, so an extremely high capacitance would occur when point charge ions are close to the surface which does not meet with the actual case.

To resolve this problem, Stern combined the Helmholtz model and Gouy-Chapman model introducing an internal Stern layer and an outer diffuse layer (Gouy-Chapman diffuse layer) [36]. In the Stern layer or called compact layer, ions are adsorbed tightly and can be divided into two regions depending on the charge polarity of ions. The inner region consists of specifically adsorbed ions; the outer region consists of not specifically adsorbed ions, as shown in Figure 2.2. Those two regions are distinguished by two planes. The inner Helmholtz plane (IHP) locates at the distance of closest specifically adsorbed anions, and the outer Helmholtz plane (OHP) locates at that of non-specifically adsorbed cations. The diffuse layer begins after OHP.

According to the structure shown in Figure 2.2(c), the EDL capacitance C_{dl} is composed of the Stern layer capacitance C_S and diffuse layer capacitance C_{diff} .

$$\frac{1}{C_{dl}} = \frac{1}{C_S} + \frac{1}{C_{diff}} \quad (2-15)$$

2.2.1.1 Activated Carbons

ACs are widely used in commercial supercapacitors because of the low cost and feasible and scalable synthesis. Porous ACs possess a large specific surface area larger than 2000 m²/g and a widely distributed pore sizes ranging from the micropores to macropores. The micropores are generally considered to be not accessible to electrolyte solutions (especially organic electrolytes), which prevent or slow down the ion transportation and limit the capacitance and energy density of supercapacitors [37]. This phenomenon can be explained by the unsuited micropore size that is too small to

accommodate electrolyte ions. To solve this drawback in ACs, controlled generation of pores with narrow distribution in mesopores range was investigated [38]. As a consequence, the pore size distribution of AC is one of the major focuses of research in EDL capacitor design. The energy density of AC-based supercapacitors is about 4-5 Wh/kg as reported [39], while the specific capacitance reaches 100-120 F/g in organic electrolytes and 150-300 F/g in aqueous electrolytes [6].

2.2.1.2 Carbon Aerogels

Compared with ACs, carbon aerogels are composed of covalently bonded carbon nanoparticles with continuous mesopores. They own surface area ranging from 400-1000 m²/g and specific capacitance from 20 to 100 F/g [40]. So there is also interest in applying carbon aerogels as the electrode material in EDL capacitor design. In addition, carbon aerogel is in a self-binded form, so there is no need to use a binder to prepare electrode. As described, carbon aerogels showed much lower ESR values than ACs. The reduced ESR leads to a high power which is the advantage of the carbon aerogel-based supercapacitors.

2.2.1.3 Carbon Nanotubes

Previously, great interest has been drawn by applying CNT as EDL electrode material. Carbon nanotube can be treated as a graphene sheet rolled up into a form, so called single-walled CNT. Single-walled CNTs have a moderate surface area up to 1300 m²/g as well as an excellent electrical conductivity up to 5000 S/cm [39]. Besides the

large surface area and electrical conductivity, the mesopores of CNT are interconnected, so that charges can distribute on almost the entire surface. Therefore, CNT-based supercapacitor can achieve a comparable capacitance, even though the CNT electrodes have a lower surface area than AC electrodes. Since ions can easily diffuse into CNT's mesopores, electrochemical cells with CNT electrodes exhibit lower ESR and higher power density than those with AC electrodes.

Enhancement on the energy density of CNT electrodes was investigated by increase the surface area through KOH activation. However, CNT-based supercapacitors are facing trade-off between high capacitance and power performance. Some efforts were taken by balancing the porosity and electrical conductivity, but they are still under further study. On the other hand, the cost of high quality single-walled CNT remains a challenge for commercialization of CNT-based supercapacitors.

2.2.1.4 Graphene

One promising candidate of the EDL supercapacitor electrode material is graphene. Graphene, due to its unique hexagonal lattice structure (shown in Figure 2.3), exhibits appealing electrical properties, chemical stability and high surface area. Experimental synthesis, firstly claimed by Andre Geim and Kostya Novoselov et al. in 2004 [41], has aroused wide interest because of its unique two dimension (2D) material structure and

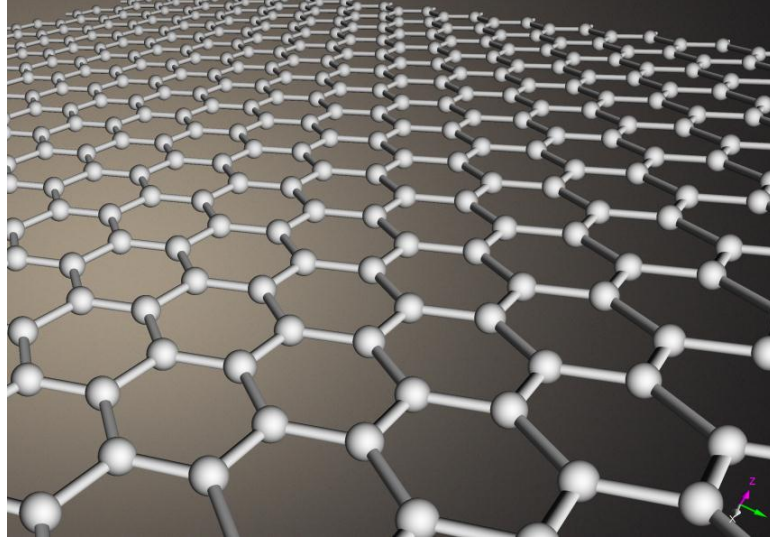


Figure 2.3 Three-dimension view of ideal graphene crystalline structure.

excellent mechanical, chemical and electrical properties, such as high thermal and electrical conductivity, quantum hall effect, large specific surface area, high carrier mobility, tunable work function, mechanical strength and chemical stability. As more and more prospect applications of graphene or graphene-based structures have been discovered and developed based on its superior mechanical, chemical and electrical properties, it is quite promising that in the near future it would draw a revolution in the electrical, semiconductor, and biochemical research and industry.

So far, a variety of methods have been developed to synthesis graphene. Among them, the impressive approaches include mechanical exfoliation of graphite [41], chemical vapor deposition of monolayer graphene [42], epitaxial growth on SiC substrate [43], unzipping of CNT [44] and so on. Generally, those methods can be classified into

two routes: growth or exfoliation. Growth methods can produce high-quality monolayer graphene, while chemical exfoliation methods are described to give the highest throughput of graphene with trade-off like layer restacking and conductivity degradation. For supercapacitors, the oxidation-reduction method can produce large-scale graphene at low cost with a large amount of exfoliated layers. In this method, graphite is heavily oxidized in presence of strong acids and oxidants with one of the Staudenmaier [45], Brodie [46] or Hummers [47] method to form a layered structure with covalently attached oxygen-containing groups (epoxide, hydroxyl, carboxyl groups). The most commonly used method is the modified Hummers method, firstly reported by Nina I. Kovtyukhova et al. in 1999 [48] which can offer high level of oxidation. The oxidation plays an important role in the whole process, and depends a lot on the selected method, reaction condition and graphite power to start with. The prepared GO powders are hydrophilic so that the intercalation of water molecules already exists [49]. One significant benefit is that GO can be easily dispersed in many solutions like water, ethanol, ethylene glycol, dimethylformamide (DMF), n-methyl-2-pyrrolidone (NMP), tetrahydrofuran (THF) at around 0.5 mg/ml [50], making it possible to process GO in liquid phase. The processability of GO colloidal suspensions is much better than graphite, and can be exfoliated into monolayer GO sheet, which can be confirmed by thickness measurements of monolayer graphene (~1nm) with atomic force microscopy (AFM) [44].

However, the resulting GO sheets generally illustrate a poor electrical conductivity owing to the effect of high disorder [52] and remaining oxygen-containing groups. A typical solution to increase the conductivity is chemical reduction, for instance, hydrazine

[53-55], dimethylhydrazine [56], hydroquinone [57], and NaBH₄ [58]. The elemental analysis with an atomic C/O ratio of 10.3 for hydrazine reduction was reported, suggesting the existence of a significant amount of retained oxygen [53] and the fact that chemically reduced graphene oxide is not the same as pristine graphene [51]. Furthermore, theoretical modeling (with a model of graphene functionalized by epoxide and hydroxyl groups) of the GO system proved that it may be difficult to reduce to below 6.25% (C:O ratio 16:1) coverage of GO in terms of removing hydroxyl groups [59]. It is consistent with most of the experimental results, and explains why it is so difficult to reduce GO to pristine graphene.

Thus, a series of methods were developed to improve both the exfoliation and reduction results. Guoxiu Wang et al. presented the graphene nanosheets achieved by ultrasonication combined with hydroquinone reduction [60]. Sungjin Park and Rodney S. Ruoff reported the tip sonication in 2009 [51], after which the exfoliated GO sheets were chemically reduced to remove the oxygen-containing groups. Hannes C. Schniepp et al. and Meihua Jin et al. published the high temperature thermal annealing above 1000 °C to achieve highly crystalline graphene [61, 62]. In 2010, Yanwu Zhu et al. claimed the microwave assisted exfoliation and reduction of GO [63]. Recently, Maher F. El-Kady et al. introduced the laser scribing methods with microfabrication capability [64].

Ideally, a monolayer of sp² bonded carbon atoms can reach specific capacitance up to ~550 F/g, large surface area of 2675 m²/g, high intrinsic mobility of 200,000 cm²/(V•s), and optical transmittance around 97.7% [65], which basically set the upper limit for all

carbon materials. The superb properties of graphene can be found by comparing with other carbon materials, as shown in Table 2.1 [66].

Materials	Specific surface area (m ² /g)	Density (g/cm ³)	Conductivity (S/cm)	Cost (H/M/L)	Aqueous electrolyte		Organic electrolyte	
					F/g	F/cm ⁻³	F/g	F/cm ⁻³
Graphite	10	2.26	10 ⁴	L	N/A	N/A	N/A	N/A
ACs	1000-3500	0.4-0.7	0.1-1	L	150 - 300	< 80	100 - 120	< 50
Carbon aerogels	400-1000	0.5-0.7	1-10	L	100 - 125	< 80	< 80	< 40
CNTs	120-500	0.6	10 ⁴ -10 ⁵	H	50-100	< 60	< 60	< 30
Graphene	2675	1-2	10 ⁶	H	100 - 205	> 100	80-110	> 80
Activated carbon fibers	1000-3000	0.3-0.8	5-10	M	120 - 370	< 150	80-200	< 120
Functionalized porous carbon	300-2200	0.5-0.9	> 300	M	150 - 300	< 180	100 - 150	< 90

Table 2.1 Comparison of different carbon materials for supercapacitors [66].

Graphene synthesized with hydrazine reduction achieved an energy density of 85.6 Wh/kg as well as a specific capacitance of 154.1 F/g [11]. Yanwu Zhu et al. exfoliate GO under microwave irradiation followed by a KOH activation to generate higher surface

area ($3100 \text{ m}^2/\text{g}$). A relatively high energy density (70 Wh/kg) and good specific capacitance (166 F/g) were observed [39]. GO was scribed by laser treatment showing a high electric conductivity (1738 S/m) and specific surface area ($1520 \text{ m}^2/\text{g}$). The electrochemical capacitors assembled with laser scribed graphene exhibited energy densities up to 1.36 mWh/cm^3 and a specific capacitance as high as 276 F/g [64]. Previously, our group investigated graphene material prepared by tip sonication combined with chemical reduction, with which an energy density value of 84.36 Wh/kg and specific capacitance of 195 F/g were observed in ionic liquid at an operating voltage of 3.5 V and a current density of 2.5 A/g . The values are comparable to most of the described research, but still can't meet the practical needs. Therefore, of special interest has been the development of more effective synthesis approaches of graphene for better electrochemical performance.

2.2.2 Pseudocapacitance

In contrast with EDL supercapacitors, pseudocapacitors store energy through a faradaic reaction at the interface between electrode and electrolyte. These faradaic reactions include electrosorption, redox reactions and intercalation processes [67, 68]. To further improve the specific capacitance of the electrode, pseudocapacitive electrode materials like conducting polymers or metal oxides were utilized to make pseudocapacitors or added to the carbon-based materials to generate hybrid supercapacitors.

2.2.2.1 Conducting Polymers

Conducting polymers, such as polyaniline (PANI), polypyrrole (PPy), poly-(3,4-ethylenedioxythiophene) (PEDOT) and derivatives of polythiophene, have a relatively higher capacitance and conductivity than carbon-based materials. Conducting polymers can store energy with not only EDL but also rapid faradic charge transfer. In general, conducting polymers are more conductive than the inorganic battery materials leading to a larger power capability. Moreover, the low ESR and manufacturing cost attracted a lot of interest into related research. However, conducting polymers are experiencing much lower cycle life than carbon electrodes because the redox sites in conducting polymer backbone are not sufficiently stable. The structure of polymer has a critical impact on the electrochemical performance by affecting the ion mobility and accessibility of pores. Thus, the design of polymer structure is important to get high charge storage efficiency and stability. Poly(Tri(4-(Thiophen-2-yl)Phenyl)Amine) (pTTPA) deposited into highly porous films or template nanotube structures yielded a remarkably high capacitance of 950 F/g in 100 mM tetrabutylammonium tetrafluoroborate in acetonitrile [69]. Graphene/CNT/PANI composites prepared via in situ polymerization exhibited the specific capacitance of 1035 F/g in 6M of KOH much higher than pure PANI capacitance [70]. Also improved cycle stability was observed in those composites, because graphene and CNT play a great role of backbone to generate a homogenous polymer distribution. It is known that conducting polymers are mechanically weak, so the composites can preserve the polymer from mechanical breaking in the long cycling [71].

2.2.2.2 Metal Oxides

Many transition metal oxides thin film including ruthenium oxide, iridium oxide, manganese oxide, cobalt oxide, nickel oxide, tin oxide, iron oxide, perovskites, ferrites etc. have been investigated as electrode material for pseudocapacitors. Because of the cost consideration, inexpensive metal oxides with good capacitive values attracted considerable attention. Unlike the asymmetric cyclic voltammetry curves of conducting polymers with current peaks at the respective redox potentials, the CV curves of metal oxides like RuO₂ and IrO₂ electrodes have a near rectangular shape, as is expected for ideal capacitors. Hydrous forms of RuO₂ have been studied intensively for supercapacitors because of the high theoretical specific capacitance limit of 1358 F/g and electrical conductivity 300 S/cm [72]. Experimental specific capacitance up to 750 F/g and 800-1200 F/g were reported for electrodeposited RuO₂ and hydrous RuO₂ /carbon composites [72, 73]. The major disadvantage of metal oxides is the low operating voltage. Materials like RuO₂ and IrO₂ can only be applied with aqueous electrolytes which set the voltage around 1V. Previously, RuO₂ electrode in H₂SO₄ electrolyte showed a maximum potential range of 1.4V [74].

2.2 Electrolytes

The key to reach high capacitance is using electrodes with high surface area and electrical conductivity. However, further researches reveal that even with high surface area materials, the device performance depends on the electrolyte as well. The performance of supercapacitors can be adjusted apparently by applying suitable

electrolytes. There are three types of electrolytes used in the supercapacitor research: aqueous electrolyte, organic electrolyte and ionic liquid. Aqueous electrolytes such as KOH, NaOH and H₂SO₄ have smaller ion size that can utilize more surface area. The conductivities of acid and alkaline solutions are advantageously high owing to the proton transport resulting in a low ESR and high power capability. However, the decomposition voltage of aqueous electrolyte is theoretically 1.23V or practically 1.3-1.4 V in kinetic terms [75]. Another concern of aqueous electrolyte is the corrosion nature of the acid or alkaline solution that may damage the electrode or other components of the device, leaving problems like reliability and self-discharge. Then, non-aqueous electrolytes were employed to break through the potential limit. Organic electrolytes, such as tetraethylammonium tetrafluoroborate and triethylmethylammonium tetrafluoroborate in acetonitrile, have been studied in supercapacitor with a relatively high potential window around 2-2.5 V. But the large organic solvent molecules set higher requirement of pore size of electrodes. And the drawbacks like electrolyte depletion upon charge and low safety also limit the use of organic electrolytes [76]. Ionic liquids, on the other hand, have an maximum operating voltage about 4-4.5V as well as a moderate ion size. AC supercapacitor cells filled with N-butyl-N-methylpyrrolidinium bis(trifluoromethanesulfonyl)imide (PYR₁₄TFSI) ionic liquid demonstrated a high cycling stability for 40000 cycles and a high stable specific capacitance of 60 F/g [77]. Hence, the choice of electrolyte depends on reliability and performance requirements of each application of supercapacitors. To choose between aqueous electrolyte, organic

electrolyte and ionic liquid, we need to consider the tradeoffs between operating voltage range, specific capacitance and ESR or power density.

Conventional supercapacitors with liquid electrolytes consist of a separator as isolation between electrodes. But there is also a trend of using solid electrolytes like poly(vinyl alcohol) (PVA)-H₃PO₄ polymer gelled electrolyte. The use of those solid electrolytes results in a simplified fabrication process with no need for separator and no possible leakage of dangerous electrolyte.

2.3 Separators

A separator works as isolation for the two electrodes to prevent the combination of ions of opposite charge. For this purpose, the separators should be ideal insulator like with high resistance. The thickness of separator would determine the capacitance value the device can achieve. Ideally, it should be very thin in range of tens of microns. To maintain a low ESR, the separator should be very porous and the pore size should be adjusted properly, so that the ions could be capable to diffuse across separator freely. Furthermore, they should be mechanically strong and chemically inert to protect the stability and conductivity of the electrolyte. The common separators used in research devices are nonwoven polypropylene (PP) membrane with a porosity of 40-60%.

2.4 Summary

This chapter has discussed the types of supercapacitors, the energy storage mechanisms and functions of each component of supercapacitors. The possible

candidates of electrodes material, electrolyte and separator are described as well as the advantages and disadvantages of them. To achieve a supercapacitor with high specific capacitance, outstanding energy density, low ESR value, long cycle life, light weight and low toxicity, graphene materials combined with ionic liquid electrolyte and PP membrane separator are the most promising approach.

Chapter 3 Synthesis of Graphene and Material

Characterization Results

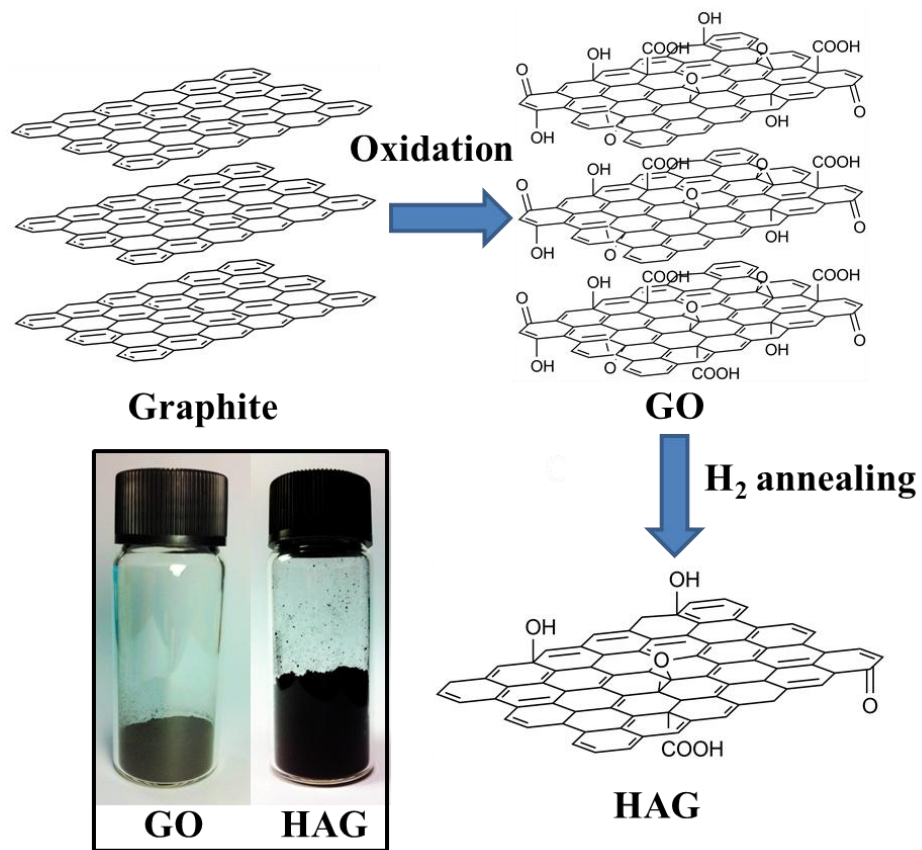


Figure 3.1 Schematic of synthesis process.

With improvements in the exfoliation and reduction techniques of graphite oxide, graphene-based materials can be produced in large-scale at low cost. A variety of oxidation-exfoliation methods have been employed to minimize the restacking effect between the graphene sheets by breaking the van der Waals force, such as chemical treatment, irradiation, thermal annealing and powerful sonication. Each of these methods has advantages and disadvantages. Several chemical treatments have been developed, but involve harmful reducing agents and are not suitable for mass production; Thermal annealing can produce high quality graphene sheets but a very high temperature of $\sim 1050^{\circ}\text{C}$ is required; the irradiation and sonication serve as a pure exfoliation techniques and always require the help of chemical reduction.

3.1 Synthesis Process

3.1.1 Preparation of graphene oxide (GO)

The schematic of synthesis process is shown in Figure 3.1. GO was prepared by oxidizing the graphite powder with modified Hummer's method. The GO is heavily oxygenated with a basal plane mainly occupied by C=O, C-OH and COOH groups.

20 g of graphite powder, 10 g of $\text{K}_2\text{S}_2\text{O}_8$ and 10 g of P_2O_5 were mixed into a solution of 30 mL concentrated H_2SO_4 at 80°C , and the mixture was allowed to react for 6 h. The product then was washed with distilled water until the pH value become neutral followed by filtration. The oxidized graphite was put into 460 mL of H_2SO_4 at 0°C using an ice bath. 60 g of KMnO_4 was added gradually with continuous stirring and cooling to keep temperature below 35°C . 920 mL of distilled water was added after 2 h. In another

2 h, 2.8 L of distilled water and 50 mL of 30% H₂O₂ stopped the reaction and the color of the solution turned into yellow. To remove metal ions, the solution was centrifuged and washed with 10% HCl and then distilled water. A two weeks dialysis was performed to completely get rid of metal ions.

3.1.2 Preparation of reduced graphene oxide (rGO)

After vacuum-drying, GO powder was put into a quartz furnace under flowing argon and heated at 200 °C. When reaching the temperature, argon was evacuated followed by introducing hydrogen gas at a pressure of 110 torr for 3 minutes. With the presence of heat, oxygen containing group would be reduced by hydrogen to form water vapor between the GO layers. When water vapor accumulates, a high pressure was generated to break the attractive forces, where the reduced GO was converted into hydrogen-annealed graphene (HAG). The process can be visually observed with the color change from brown to black (related to reduction) and large volume expansion (related to exfoliation). It is worth to mention that the reduction and exfoliation happen simultaneously in this approach avoiding separate treatment for each of them.

3.2 Material Characterization

3.2.1 Scanning electron microscopy

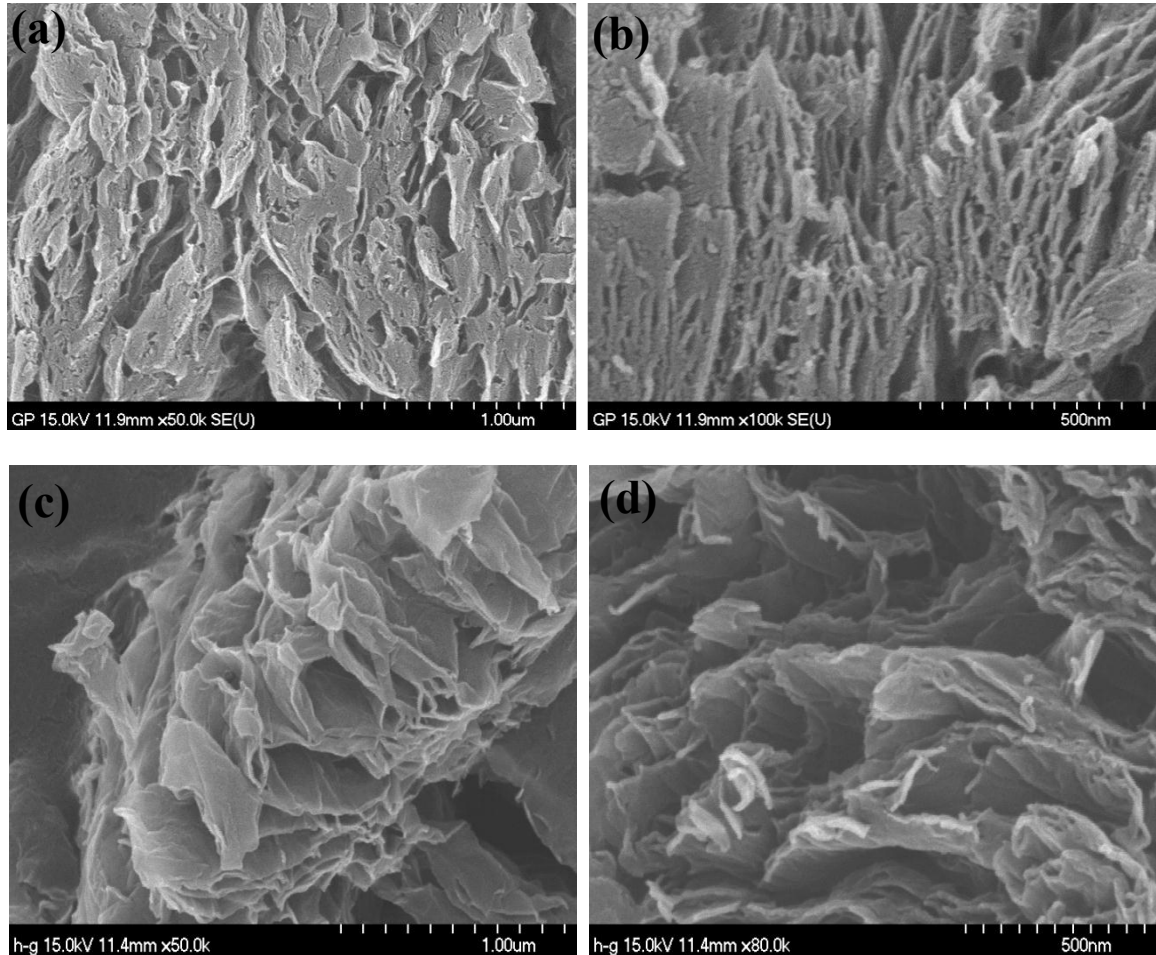


Figure 3.2 (a) and (b) are scanning electron microscopy images at low and high magnification, (c) and (d) are field emission scanning electron microscopy images of HAG sample.

Scanning electron microscopy (SEM) utilizes a condensed and focused electron beam to scan a sample generating detectable signal to produce image. The SEM and field emission scanning electron microscopy (FESEM) images show the typical cross section of HAG surface. As seen in Figure 3.2, the graphene sheets have been homogeneously exfoliated. The wrinkled structure is the result of fast removal of oxygen containing groups. It reveals the successful exfoliation under which a large area of restacking layers has been peeled off so that it shows obvious gaps between them. Thus, HAG maintains a mesoporous structure with pore size around 4 nm obtained from low-temperature nitrogen isothermal adsorption.

3.2.2 Transmission electron microscopy

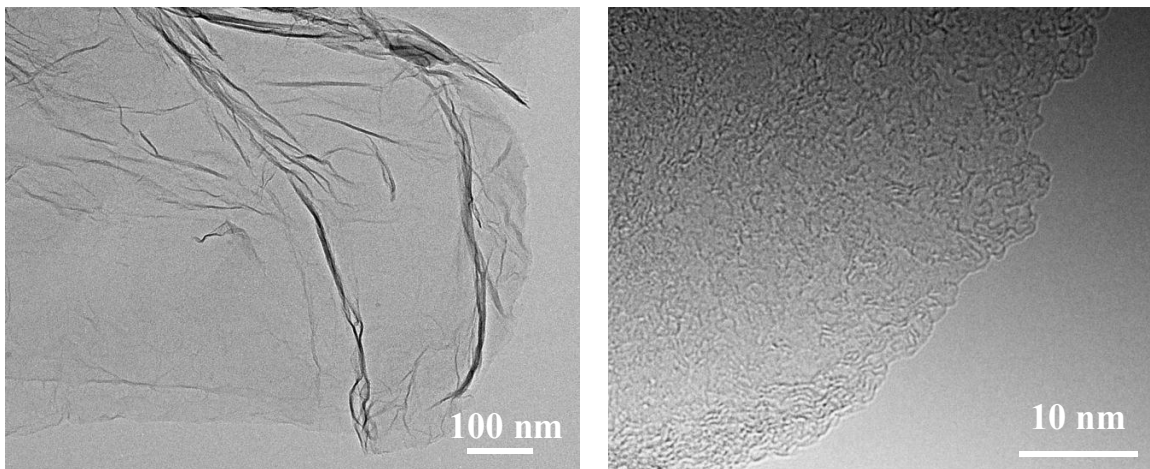


Figure 3.3 Transmission electron microscopy images of HAG sample.

The transmission electron microscopy (TEM) images (Figure 3.3) again show the morphology of HAG powder, where the agglomeration is very limited. To prepare sample for TEM, a very limited amount of HAG powder was dispersed into ethanol. After 2 h's sediment, the suspension was drop-casted on a copper grid. Then TEM analysis can be performed on the dried copper grid. The edge of the sheet showed much less restacked structure, although overlapped area of graphene sheet was observed in some region. It suggests that the graphene has been recovered to some extent after hydrogen annealing. The winkled surface would be beneficial for electrolyte ions to access. Hence, a device can be made with lightweight and highly porous HAG electrodes.

3.2.3 Nitrogen isothermal adsorption measurement

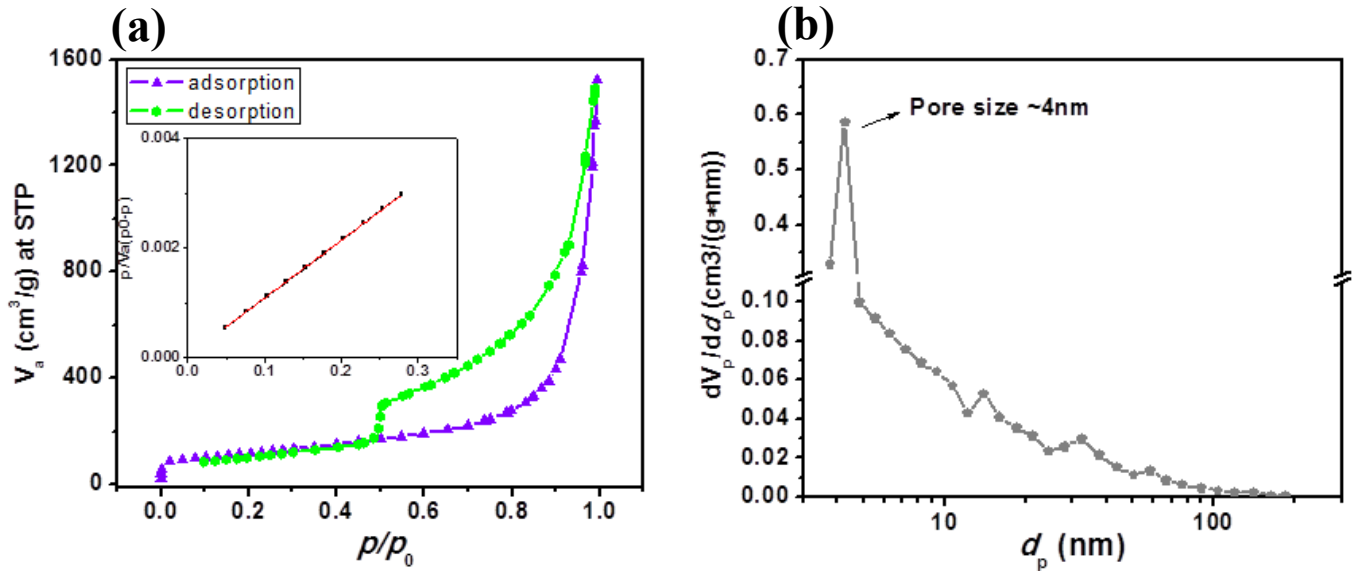


Figure 3.4 (a) Nitrogen adsorption/desorption analysis of HAG sample, (b) Pore size distribution versus the pore width.

For powders and porous solid materials, the study of nitrogen isothermal adsorption experiment would reveal the surface area and porosity. Figure 3.4(a) displays a type IV adsorption isothermal curve with a hysteresis loop generally exhibited by mesoporous solids, based on which the Brunauer-Emmett-Teller (BET) and Barret-Joyner-Halenda (BJH) methods are applied. The hysteresis loop between adsorption and desorption along with a sharp fall at high relative pressure implies the near cylindrical or slit geometry of major mesopores, which appears to be in good agreement with the electron microscopy images. The HAG demonstrates a BET specific surface area of $410 \text{ m}^2/\text{g}$, which is extracted from the linear region of $1/[V_a(p_0/p-1)]$ versus p/p_0 in the classical BET range of 0.05-0.3 (inset of Figure 3.4 (a)). Figure 3.4(b) shows differential pore volume per unit mass as a function of pore size, extracted with BJH method. A peak corresponding to a pore volume of $2.46 \text{ cm}^3/\text{g}$ occurs at pore size of 4.27 nm. It is desired to adapt the pores size to electrolyte ions size for optimizing the capacitance and the energy density. Special consideration regarding the size difference between anion and cation adsorbed at positive and negative electrodes is also necessary. As a support to it, the damage extent of the two electrodes after long charge-discharge cycles varies a lot, where one electrode would remain a whole piece and the other becomes fragmentary with loosen pieces. Since most of the pores exhibit larger size than the electrolyte ions, ions can accommodate inside the HAG electrodes leading to better electrolyte accessibility. This porous surface would allow electrolyte to access the interior region even when compressed to electrode.

3.2.3 X-ray diffraction

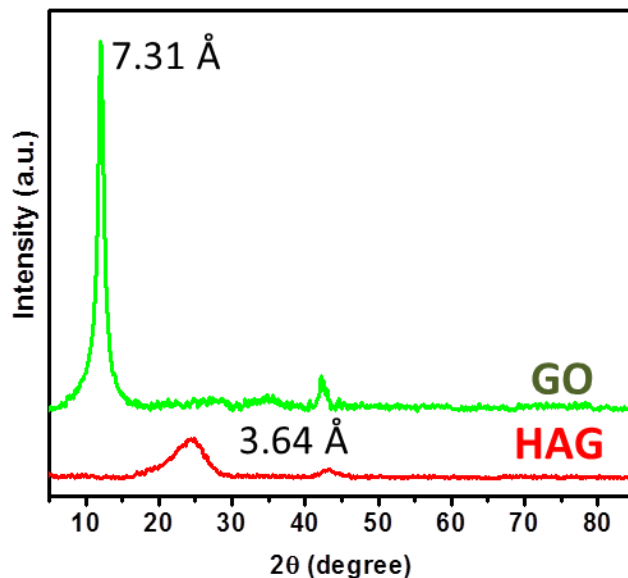


Figure 3.5 X-ray diffraction patterns of GO and HAG.

The X-ray diffraction (XRD) features of GO and HAG are presented in Figure 3.5. The intense (002) peak of GO occurs at 12.06° with a d-spacing of 7.31 \AA . Upon the hydrogen treatment, GO diffraction peak disappears and a new peak with reduced intensity and broadened width appears around 24.44° . The interlayer spacing of the reduced product decreases to a much smaller value of 3.64 \AA which suggests the removal of oxygen containing groups by reaction with hydrogen molecules under heat. Compared with the interlayer distance of graphite $\sim 3.35 \text{ \AA}$ [78], the shift implies that there are some

residual functional groups left. And the appearance of broad peak is an indication of a loss of order in HAG.

3.2.3 Raman spectrum

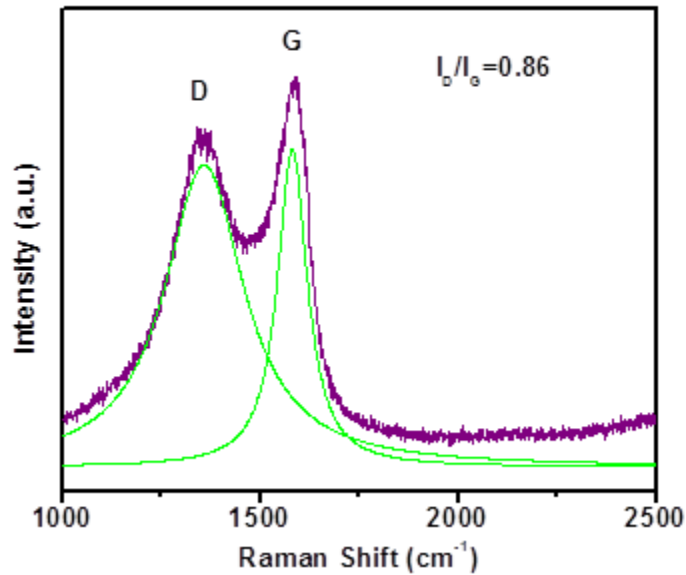


Figure 3.6 Raman spectrum of HAG.

The typical Raman features of graphene are the D-band around 1350 cm⁻¹ and the G-band around 1580 cm⁻¹ [79]. For a monolayer or less stacked graphene, an intense 2D-band caused by second order of zone-boundary phonons is expected to be observed at about 2700 cm⁻¹ [79]. Figure 3.6 shows the Raman spectrum of HAG sample. After Lorentzian fitting, the D-band caused by disordered structure can be found approximately

at 1350.96 cm^{-1} . It is pretty common that the oxidation approaches generate a certain amount of defects in graphene sheets. The G-band corresponding to E_{2g} mode at the center of Brillouin zone locates at $\sim 1582.85\text{ cm}^{-1}$. The intensity ratio of D/G bands is often used as prediction of defects in samples. The ratio of HAG D-band and G-band, I_D/I_G , is around 0.86 less than 1.0, indicating the partial restoring of the π -conjugated structure.

3.2.3 X-ray photoelectron spectra

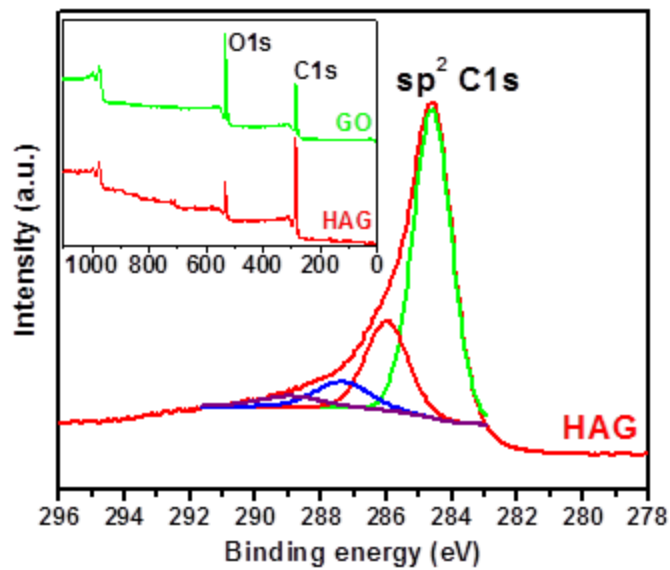


Figure 3.7 X-ray photoelectron spectra of GO and HAG.

The reduction result was characterized by X-ray photoelectron spectroscopy (XPS) and Fourier transform infrared spectroscopy (FTIR) measurement. In the XPS spectrum (Figure 3.7), the C/O ratio increases from ~2 to ~5 with O1s peak reduced significantly from GO to HAG. By performing Gaussian-Lorentzian fitting, the intense C-C peak is observed at binding energy of 284.6 eV showing the sp^2 bonding. The broad tail towards higher binding energy up to 296 eV is because of the contributions of various carbon bonding configurations. Those multiple peaks at 285.99, 287.37, 288.93 eV are typically assigned for oxygen containing groups C-OH (or C-O-C), C=O and O=C-OH (COOH) respectively [80]. The existence of C-O-C which is widely seen in the graphene oxide system has a similar C1s binding energy to C-OH [81].

3.2.3 Fourier transform infrared spectrum

Another confirmation of the reduction mechanism is obtained by the FTIR spectrum. In HAG, the broad and intense peak at 3433 cm^{-1} and 1637 cm^{-1} [82] correspond to the OH stretching in water molecules indicating that there are lots of H_2O generated after reduction. This phenomenon is consistent with our hypothesis of hydrogen reduction with water vapor as reaction product. Moreover, the C=C stretching

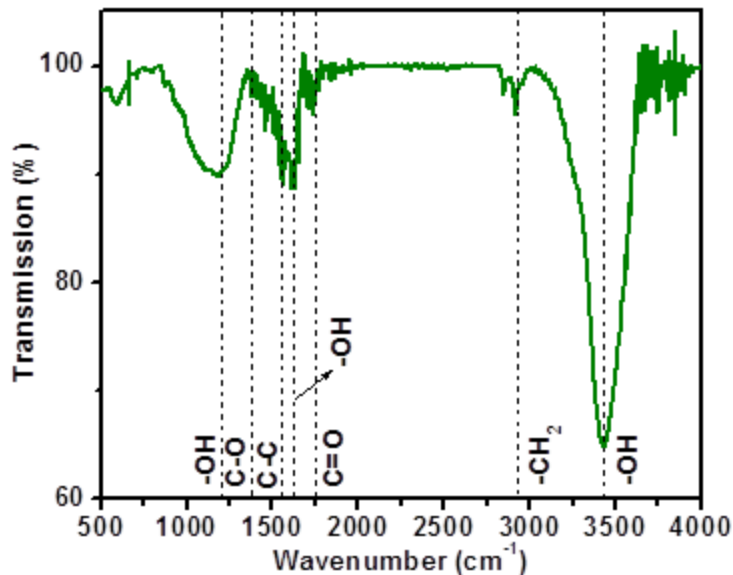


Figure 3.8 Fourier transform infrared spectrum of HAG.

is observed at 1560 cm^{-1} . Other than the two peaks, the peaks at 1719 cm^{-1} , 1383 cm^{-1} and 1190 cm^{-1} related to the C=O, C-O and -OH of O=C-OH (COOH) [83] show small intensities which suggest removal of those function groups. The asymmetric and symmetric stretching peaks of $-\text{CH}_2$ at 2918 cm^{-1} and 2851 cm^{-1} imply the restoration of carbon basal planes owing to hydrogen reduction [82, 84].

3.3 Conclusion

In this chapter, the reduced graphene oxide was synthesized by an oxidation-reduction technique in which the hydrogen annealing works as a combination of exfoliation and reduction process. It is a rapid synthesis which provides mass-production

capability. The material was characterized by SEM, TEM, nitrogen isothermal adsorption, XRD, Raman spectroscopy, XPS and FTIR. These characterization results reveal two facts: 1. after hydrogen annealing the restacking of graphene layers is limited which suggest a successful exfoliation; 2. most of the oxygen-containing groups (epoxide, hydroxyl and carboxyl groups) have been considerably removed during the reduction reaction with hydrogen gas forming water vapor. Reasonable quality graphene sheets were obtained by using a simple method that can be easily scaled up to meet the industrial requirements.

Chapter 4 Supercapacitor Assembly and Electrochemical Measurements

4.1 Supercapacitor assembly

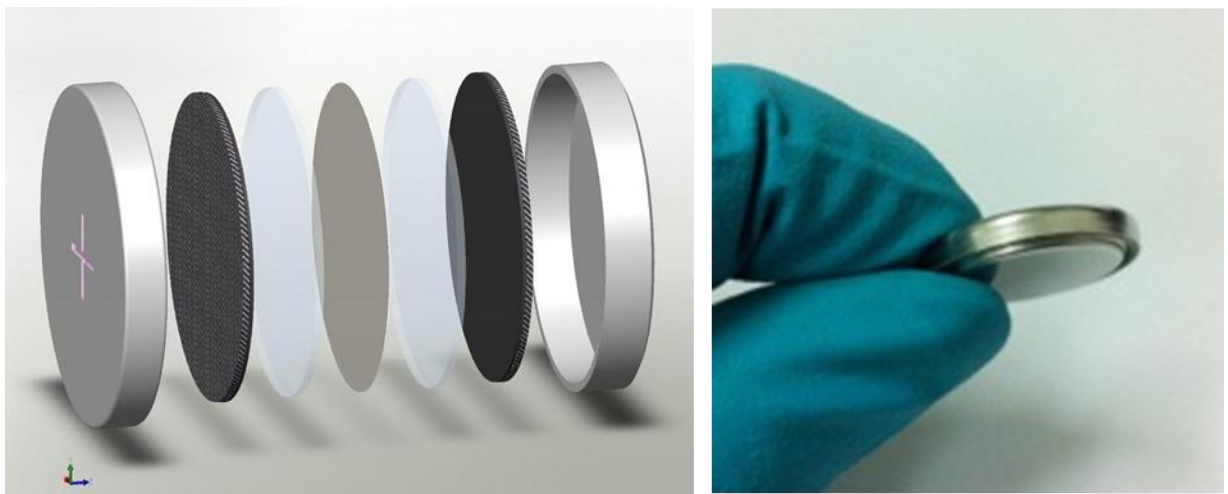


Figure 4.1 Schematic of the symmetrical supercapacitor structure and image of the assembled device.

To evaluate the electrochemical performance of HAG electrodes, supercapacitors were assembled in symmetrical cell geometry with two electrodes (Figure 4.1). To

prepare the electrode, graphene material was mixed with binder and conducting additive and pressed to a nickel mesh as current collector. The coin-cell type devices were assembled with two HAG electrodes in a glovebox. The devices were measured with ionic liquid 1-Ethyl-3-methylimidazolium tetrafluoroborate (EMIMBF₄) and LiPF₆ electrolytes respectively.

4.2 Electrochemical performance of the graphene electrodes

4.2.1 Cyclic Voltammetry

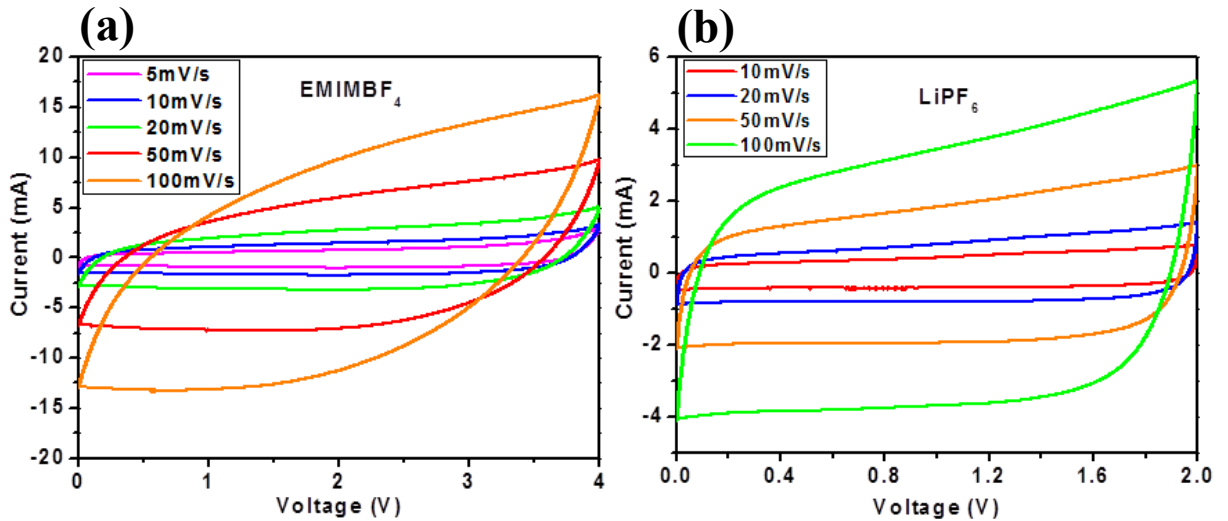


Figure 4.2 Cyclic voltammetry curves for HAG supercapacitors with (a) ionic liquid and (b) LiPF₆ electrolyte at different scan rates.

When capacitance C is fixed with swept voltage, current will retain constant value because of the relation $I(t)=C(dV/dt)=C*s$ [75]. Therefore, the resulted cyclic

voltammetry curves of ideal capacitors are expected to display rectangular current response, if the same scan rate dV/dt is applied in forward and reverse directions of the sweep. The CV curves of HAG electrodes in EMIMBF₄ and LiPF₆ are nearly rectangular shape from scan rate 10 mV/s to 100 mV/s indicating capacitive behavior (Figure 4.2(a) and (b)). The electrochemical performance of supercapacitors also depends on the nature of electrolyte. Aqueous electrolytes, like KOH and H₂SO₄, generally have smaller ion size and lower equivalent series resistance (ESR) compared with ionic liquid, but lower breakdown voltage. The ionic liquid EMIMBF₄ can work under high voltage up to 4.3 - 4.5 V [11, 85], which will bring significant benefits in improvement of energy density.

4.2.2 Galvanostatic charge-discharge

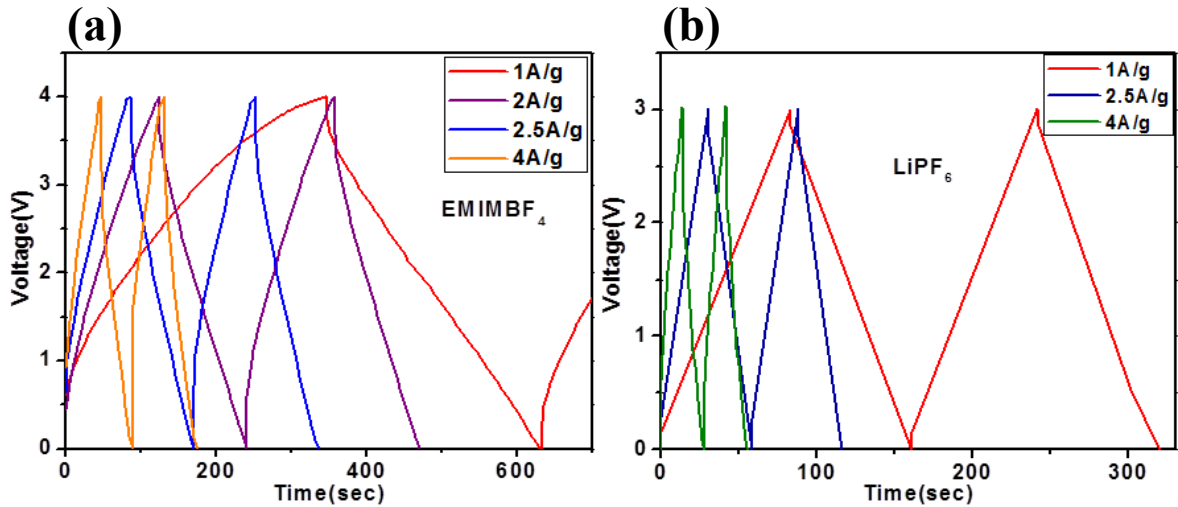


Figure 4.3 galvanostatic charge-discharge curves of HAG supercapacitors with (a) ionic liquid and (b) LiPF₆ electrolyte at different current densities.

The galvanostatic charge-discharge (GCD) measurements were taken at various current densities, shown in Figure 4.3. The nearly linear discharging curves illustrate an ideal EDL capacitor performance which can be found in $dV/dt=I/C$. The abrupt voltage drop at the beginning of discharging is due to the voltage loss across the ESR. GCD resembles the way how a load is connected with a supercapacitor in most of the applications, so that it is widely accepted as a reliable method to determine the capacitance and energy density of supercapacitors. The equation 4-1 is used to extract the specific gravimetric capacitance [39].

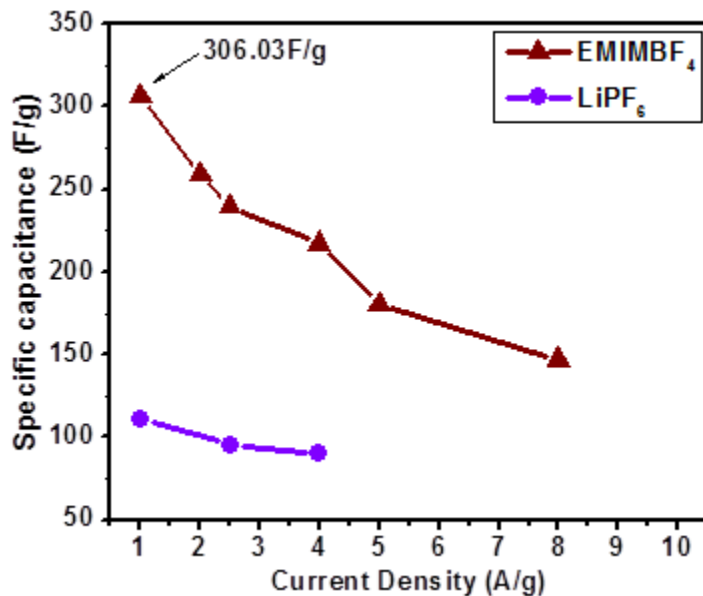


Figure 4.4 Specific capacitances of HAG supercapacitors calculated from GCD curves at various current densities.

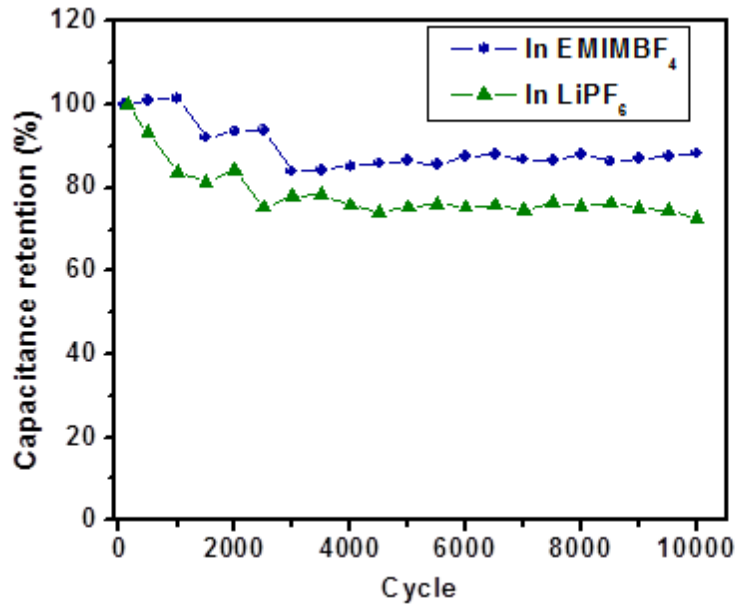


Figure 4.5 Cycling stability of the HAG supercapacitors after 10000 cycles.

$$C_s = \frac{4C}{m} = \frac{4I\Delta t}{m\Delta V} \quad (4-1)$$

where C is the measured capacitance of the two-electrode cell, I is the constant current, Δt is the discharging time (except the donation of ESR), m is the total weight of electrode

materials and ΔV is the voltage drop during discharging process (except the voltage drop on ESR). The typical specific capacitance of graphene supercapacitors in ionic liquid is in the range of 100-250 F/g. The specific capacitance values of ionic liquid extracted from discharge curves are 306.03, 256.19, 239.47, 216.99, 180.30, and 146.77 F/g at current densities of 1, 2, 2.5, 4, 5, and 8 A/g.

As seen in Figure 4.4, the capacitances of LiPF_6 at the same current densities are much smaller as a result of the natural properties and different breakdown voltage limits of electrolytes. After charging and discharging for 10,000 cycles (Figure 4.5), 88% of the specific capacitance is retained which confirms the stability of HAG supercapacitor.

4.2.3 Electrochemical impedance spectroscopy

The electrochemical impedance studies are shown in Figure 4.6. Nyquist plots show a semicircle in high frequency region and a straight line in the low frequency region. Compared with LiPF_6 , the more vertical line of ionic liquid proves a nearly ideal capacitive response. The ESR obtained from the x-intercept of Nyquist plot is 4.26 ohm. The low value means that the mesoporous graphene can deliver a high power density despite of the viscosity of ion liquid.

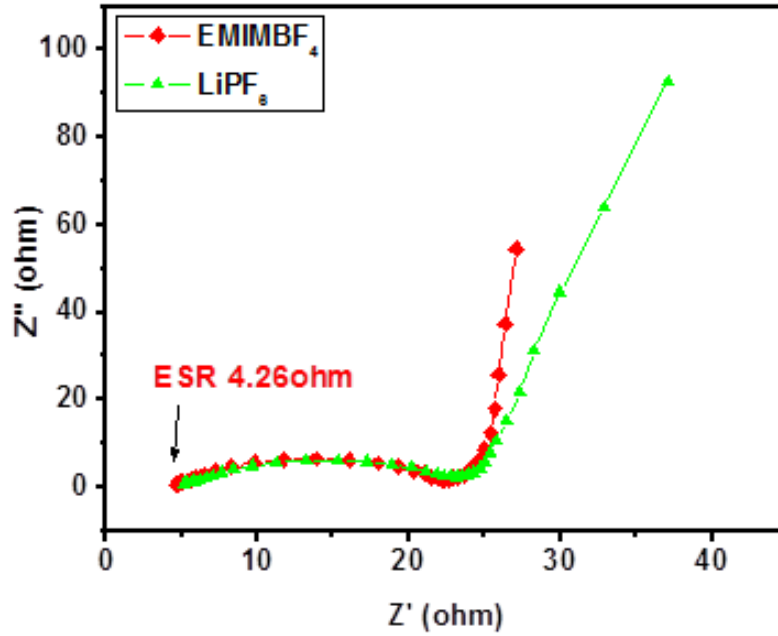


Figure 4.6 Nyquist plot for HAG supercapacitors.

4.2.4 Energy density and power density

Based on equation 1-5, the energy densities at different current densities were obtained using the following formula [11, 39]:

$$E = \frac{1}{2}(C/m)V^2 = \frac{1}{8}C_s V^2 \quad (4-2)$$

The corresponding power density was calculated according to [11]:

$$P = \frac{E}{\Delta t} \quad (4-3)$$

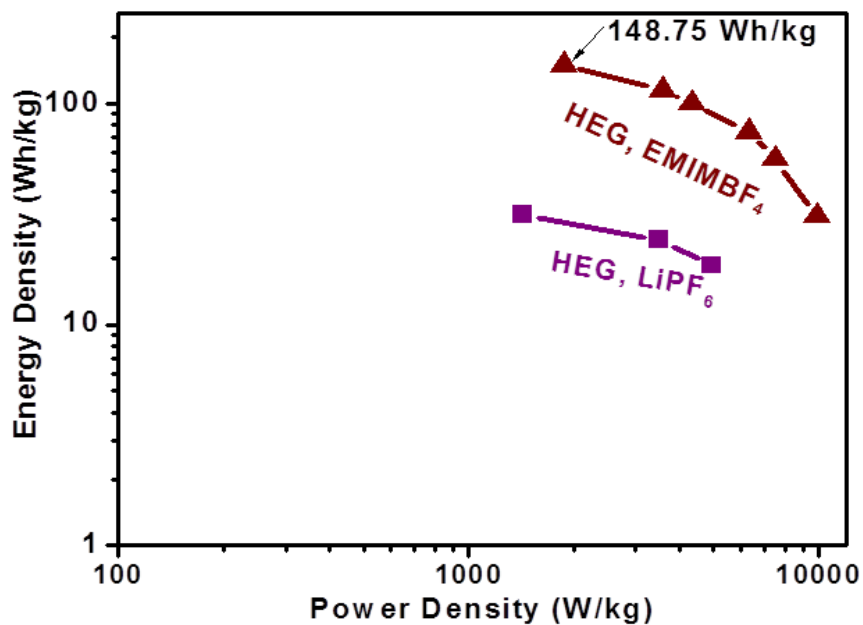


Figure 4.7 Ragone plot of the HAG supercapacitors.

To verify the relationship between energy and power density, the Ragone plot is given in Figure 4.7. An ultra-high energy density of 148.75 Wh/kg at 1 A/g was achieved with ionic liquid at room temperature. For comparison, previous reported values of graphene supercapacitor are between 10-90 Wh/kg at 1A/g, and the energy density of lithium-ion batteries is in the range of 100-160 Wh/kg. In addition, the highest power density of 9854.49 W/kg was obtained at 8A/g suggesting that the HAG supercapacitor is suitable for peak-power applications. The outstanding performance of ionic liquid electrolyte is further proved with comparison to LiPF₆ in Ragone plot.

Material	Electrolyte	Current density	Specific capacitance	Energy density	Reference
Curved graphene	Ionic liquid	1A/g	154.1F/g	85.6Wh/kg	11
a-MEGO	Organic electrolyte	5.7A/g	166F/g	~70Wh/kg	39
LSG	Organic electrolyte	5A/g	276F/g	1.36Wh/L	64
EM-CCG film	Organic electrolyte	1A/g	167.1F/g	110.3Wh/L	86
HAG (This work)	Ionic liquid	1A/g	306.03F/g	148.75Wh/kg	

Table 4.1 Performance comparison of reported graphene-based supercapacitors

4.3 Conclusion

In this chapter, CV, GCD and electrochemical impedance results were demonstrated. The near rectangular CV curves with ionic liquid and LiPF₆ at scan rate of 100mV/s suggested very efficient charge transfer within the porous graphene electrodes. The triangle charge-discharge responses with a little voltage drop indicated an ideal capacitor performance. And the vertical spike in low frequency region of Nyquist plot verified the capacitive behavior again. The values of specific capacitance, energy density and power density were extracted from the charge-discharge curves. Utilizing ionic liquid, the device achieved a high specific capacitance which is 56% of the theoretical upper limit (550 F/g). A high power density of 9854 W/kg was achieved with a reasonable energy density of 30 Wh/kg. The excellent electrochemical performance of HAG electrodes is due to the good compatibility between the hydrogen annealed graphene material and the applied electrolyte.

Previously, graphene-based supercapacitors have been researched with various electrolytes to improve the energy density. However, to the best of our knowledge, there has been no report on a graphene-based EDL supercapacitor illustrating an energy density comparable to the commercialized lithium-ion batteries at room temperature. Chenguang Liu et al. prepared the supercapacitor with chemically reduced graphene in EMIMBF₄ electrolyte resulting in an energy density of 85.9 Wh/kg at 1 A/g [11]. Yanwu Zhu et al. used chemical activation of microwave exfoliated graphite oxide to synthesize a porous graphene material with high surface area and electric conductivity, with which a supercapacitor in BMIMBF₄/AN electrolyte achieved a specific capacitance of 166 F/g and an energy density of ~70 Wh/kg at 5.7 A/g [39]. Maher F. El-Kady et al. presented laser scribing method with which the graphene-based supercapacitor encapsulated in ionic liquid offered specific capacitance of 276 F/g (5.02 mF/cm²) and an energy density of 1.36 mWh/cm² [64].

Chapter 5 Conclusions and Future Work

To conclude, the porous graphene material was synthesized by a scalable annealing method involving a rapid and efficient annealing process. The resulted HAG is proved by multiple characterization results to offer prescribed surface morphology, specific surface area, pore size, limited restacking and highly reduced structure. Due to its outstanding physical and chemical properties, HAG plays a good role as electrode material, and makes it possible to produce high-performance supercapacitor with energy density and EDL capacitance.

The supercapacitor device is assembled and measured in a symmetrical structure with two HAG electrodes. The specific capacitance of 306.03 F/g and energy density of 148.75 Wh/kg at 1A/g were realized with HAG supercapacitor at the current density of 1 A/g. Meantime, the power density extracted at 8A/g reaches ~10k W/kg. Compared with previously investigated carbon-based EDL capacitors, the HAG supercapacitor is a milestone in terms of capacitance and energy density. Moreover, the HAG supercapacitors show excellent stability for more than 10,000 charge-discharge cycles.

Although this template approach has been confirmed to be very effective, the quality of produced graphene still needs to be improved. To achieve this, novel synthesis

methods will be explored such as irradiation, plasma treatment, chemical activation, thermal annealing and so on. Some biological carbon materials also deserve attention because of their natural porous structure and easy access. It is critical to find the balance point between cost and performance. As to the supercapacitor research, alternations or improvements in the electrode preparation, device structure, electrolyte selection and packaging method are under research.

In the near future, it is quite possible that a supercapacitor device with comparable energy density to lithium ion battery would be introduced into market. This energy storage device will bring a technical revolution for the century with their superb features.

References

- [1]. G. Wang, L. Zhang and J. Zhang, A review of electrode materials for electrochemical supercapacitors, *Chem. Soc. Rev.*, 41, pp. 797-828, 2012.
- [2]. M. Armand and J. M. Tarascon, Building better batteries, *Nature*, 451, pp. 652-657, 2008.
- [3]. H. Wu, G. Yu, L. Pan, N. Liu, M. T. McDowell, Z. Bao and Y. Cui, Stable Li-ion battery anodes by in-situ polymerization of conducting hydrogel to conformally coat silicon nanoparticles, *Nature Communications*, 4, 1943, 2013.
- [4]. C. M. Park, J. H. Kim, H. Kimc and H. J. Sohn, Li-alloy based anode materials for Li secondary batteries, *Chem. Soc. Rev.*, 39, pp. 3115-3141, 2010.
- [5]. J. R. Miller, P. Simon, Electrochemical Capacitors for Energy Management, *Science* 321, pp. 651-652, 2008.
- [6]. P. Simon, Y. Gogotsi, Materials for electrochemical capacitors, *Nat. Mater.* 7, 845 (2008).
- [7]. A. Burke, Ultracapacitors: Why, How, and Where is the Technology, *J. Power Sources* 91, pp. 37-50, 2000.
- [8]. M. S. Halper, J. C. Ellenbogen, *Supercapacitors: A Brief Overview*, MITRE, 2006.

- [9]. D. Qu, Studies of the activated carbons used in double-layer supercapacitors, *J. Power Sources* 109, pp. 403-411, 2002.
- [10]. J.A. Fernández, T. Morishita, M. Toyoda, M. Inagaki, F. Stoeckli, T.A. Centeno, Performance of mesoporous carbons derived from poly(vinyl alcohol) in electrochemical capacitors, *J. Power Sources*, 175, pp. 675-679, 2008.
- [11]. C. Liu, Z. Yu, D. Neff, A. Zhamu, and B. Z. Jang, Graphene-based supercapacitor with an ultrahigh energy density, *Nano Lett.*, 10, pp. 4863-4868, 2010.
- [12]. Comparison of Fuel Cell Technologies, U.S. Department of Energy, Energy Efficiency and Fuel Cell Technologies Program, February 2011
- [13]. A. Dupuis, Proton exchange membranes for fuel cells operated at medium temperatures: Materials and experimental techniques, *Progress in Materials Science*, 56, pp. 289-327, 2011.
- [14]. R. Kotz, and M. Carlen, Principles and applications of electrochemical capacitors, *Electrochimica Acta*, 45, pp. 2483-2498, 1999.
- [15]. W. Henson, Optimal battery/ultracapacitor storage combination, *J. Power Sources*, 179, pp. 417-423, 2008.
- [16]. P. Bubna, S. G. Advani, A. K. Prasad, Integration of batteries with ultracapacitors for a fuel cell hybrid transit bus, *Journal of Power Sources*, 199, pp. 360-366, 2012.
- [17]. S. Knoth, 2-A supercap charger balances and protects cells in portable applications, *Power-eetimes*, 222901984, 2010.

- [18]. J. R. Miller and A. F. Burke, Electrochemical Capacitors: Challenges and Opportunities for Real-World Applications, The Electrochemical Society Interface Spring 2008, pp. 53-57, 2008.
- [19]. J. P. Meyers, Getting Back Into Gear: Fuel Cell Development after the Hype, The Electrochemical Society Interface Winter 2008, pp. 36–39, 2008.
- [20]. O. J. Murphy and A. Cisar, E. Clarke, Low-cost light weight high power density PEM fuel cell stack, *Electrochimica Acta*, 43, pp. 3829–3840, 1998.
- [21]. A. Burke, R&D considerations for the performance and application of electrochemical capacitors, *Electrochimica Acta*, 53, pp. 1083-1091, 2007.
- [22]. H. Pan, J. Li and Y. Feng, Carbon Nanotubes for Supercapacitor, *Nanoscale Res Lett.*, 5(3), pp. 654-668, 2010.
- [23]. G. A. Snook, P. Kaob, and A. S. Best, Conducting-polymer-based supercapacitor devices and electrodes, *J. Power Sources*, 196, pp. 1–12, 2011
- [24]. C.D. Lokhandea, D.P. Dubala, and Oh-Shim Joo, Metal oxide thin film based supercapacitors, *Current Applied Physics*, 11, pp. 255–270, 2011.
- [25]. X. Lang, A. Hirata, T. Fujita and M. Chen, Nanoporous metal/oxide hybrid electrodes for electrochemical supercapacitors, *Nature Nanotechnology*, 6, pp. 232–236, 2011.
- [26]. R. B. Rakhi, W. Chen, D. Chaa and H. N. Alshareef, High performance supercapacitors using metal oxide anchored graphene nanosheet electrodes, *J. Mater. Chem.*, 21, pp. 16197-16204, 2011.

- [27]. J. R. Lake, A. Cheng, S. Selverston, Z. Tanaka, J. Koehne¹, M. Meyyappan, and B. Chen, Graphene metal oxide composite supercapacitor electrodes, *J. Vac. Sci. Technol. B*, 30, pp. 03D118-03D118-6, 2012.
- [28]. F. Zhang, T. Zhang, X. Yang, L. Zhang, K. Leng, Y. Huang and Y. Chen, A high-performance supercapacitor-battery hybrid energy storage device based on graphene-enhanced electrode materials with ultrahigh energy density, *Energy Environ. Sci.*, 6, pp. 1623-1632, 2013.
- [29]. K. Karthikeyana, V. Aravindanb, S.B. Leea, I.C. Janga, H.H. Lima, G.J. Parkc, M. Yoshioc, and Y.S. Lee, Electrochemical performance of carbon-coated lithium manganese silicate for asymmetric hybrid supercapacitors, *J. Power Sources*, 195, pp. 3761–3764, 2010.
- [30]. L. L. Zhang and X. S. Zhao, Carbon-based materials as supercapacitor electrodes, *Chem. Soc. Rev.*, 38 , pp. 2520–2531, 2009.
- [31]. H. Helmholtz, Ueber einige Gesetze der Verteilung elektrischer Strome in körperlichen Leitern mit Anwendung auf die thierisch-elektrischen Versuche, *Pogg. Ann. Phys. Chemie*, 89, pp. 211-233, 1853.
- [32]. G. Gouy, Sur la Constitution de la Charge Electrique a la Surface d'un Electrolute, *J. Phys.*, 9, pp. 457-468, 1910.
- [33]. D. L. Chapman, LI. A contribution to the theory of electrocapillarity, *Phil.Mag.*, 25, pp. 475-481, 1913.
- [34]. E.J.W. Verwey and J.Th.G. Overbeek, *Theory of the Stability of Lyophobic Colloids*, Elsevier Publishing Company Inc., 1948.

- [35]. S. Engstrom and H. Wennerstrom, Ion condensation on planar surfaces. A solution of the Poisson-Boltzmann equation for two parallel charged plates, *J. Phys. Chem.*, 82, pp. 2711–2714, 1978.
- [36]. O. Stern, Zur Theorie der Elektrolytischen Doppelschicht, *Z. Electrochem*, 30, pp. 508-516, 1924.
- [37]. K. L. Yang, S. Yiacoumi, and C. Tsouris, Electrosorption capacitance of nanostructured carbon aerogel obtained by cyclic voltammetry, *J. Electroanal. Chem.*, 540, pp. 159-167, 2003.
- [38]. H. Zhou, S. Zhu, M. Hibino, and I. Honma, Electrochemical capacitance of self-ordered mesoporous carbon, *J. Power Sources*, 122, pp. 219-223, 2003.
- [39]. Y. Zhu, S. Murali, M. D. Stoller, K. J. Ganesh, W. Cai, P. J. Ferreira, A. Pirkle, R. M. Wallace, K. A. Cychoz, M. Thommes, D. Su, E. A. Stach, R. S. Ruoff, Carbon-Based Supercapacitors Produced by Activation of Graphene, *Science* 332, pp. 1537-1541, 2011.
- [40]. P. Simon, A. Burke, Nanostructured Carbons: Double-Layer Capacitance and More, *The Electrochem. Soc. Interface Spring 2008*, pp. 38-43, 2008.
- [41]. K. S. Novoselov, A. K. Geim, S. V. Morozov, D. Jiang, Y. Zhang, S. V. Dubonos, I. V. Grigorieva, A. A. Firsov, Electric Field Effect in Atomically Thin Carbon Films, *Science*, 306, pp. 666-669, 2004.
- [42]. K. S. Kim, Y. Zhao, H. Jang, S. Y. Lee, J. M. Kim, K. S. Kim, J. H. Ahn, P. Kim, J. Y. Choi and B. H. Hong, Large-scale pattern growth of graphene films for stretchable transparent electrodes, *Nature*, 457, pp. 706-710, 2009.

- [43]. K. V. Emtsev, A. Bostwick, K. Horn, J. Jobst, G. L. Kellogg, L. Ley, J. L. McChesney, T. Ohta, S. A. Reshanov, J. Röhrl, E. Rotenberg, A. K. Schmid, D. Waldmann, H. B. Weber and T. Seyller, Towards wafer-size graphene layers by atmospheric pressure graphitization of silicon carbide, *Nature Materials*, 8, pp. 203–207, 2009.
- [44]. D. V. Kosynkin, A. L. Higginbotham, A. Sinitskii, J. R. Lomeda, A. Dimiev, B. K. Price and J. M. Tour, Longitudinal unzipping of carbon nanotubes to form graphene nanoribbons, *Nature*, 458, pp. 872-876, 2009.
- [45]. L. Staudenmaier, Verfahren zur Darstellung der Graphitsäure, *Ber. Deut. Chem. Ges.* 31, pp. 1481-1499, 1898.
- [46]. B.C. Brodie, Sur le poids atomique du graphite, *Ann. Chim. Phys.*, 59, pp. 466-472, 1860.
- [47]. W. S. Hummers and R. E. Offeman, Preparation of graphitic oxide, *J. Am. Chem. Soc.*, 80, pp. 1339-1339, 1958.
- [48]. N. I. Kovtyukhova , P. J. Ollivier, B. R. Martin, T. E. Mallouk, S. A. Chizhik, E.V. Buzaneva, and A. D. Gorchinskiy, Layer-by-Layer Assembly of Ultrathin Composite Films from Micron-Sized Graphite Oxide Sheets and Polycations, *Chem. Mater.*, 11, pp. 771–778, 1999.
- [49]. A. Buchsteiner, A. Lerf and J. Pieper, Water dynamics in graphite oxide investigated with neutron scattering, *J. Phys. Chem. B*, 110, pp. 22328–22338, 2006.
- [50]. J. I. Paredes, S. Villar-Rodil, A. Martinez-Alonso, and J. M. D. Tascón, Graphene oxide dispersions in organic solvents. *Langmuir*, 24, pp. 10560–10564, 2008.

- [51]. S. Park and R. S. Ruoff, Chemical methods for the production of graphenes, *nature nanotechnology*, *Nature Nanotechnology*, 4, pp. 217–224, 2009.
- [52]. I. Jung, D. A. Dikin, R. D. Piner, and R. S. Ruoff, Tunable Electrical Conductivity of Individual Graphene Oxide Sheets Reduced at “Low” Temperatures, *Nano Lett.*, 8, pp. 4283–4287, 2008.
- [53]. S. Stankovich, D. A. Dikin, R. D. Piner, K. A. Kohlhaas, A. Kleinhammes, Y. Jia, Y. Wu, S. T. Nguyen, R. S. Ruoff, Synthesis of graphene-based nanosheets via chemical reduction of exfoliated graphite oxide, *Carbon*, 45, pp. 1558–1565, 2007.
- [54]. V. C. Tung, M. J. Allen, Y. Yang and R. B. Kaner, High-throughput solution processing of large-scale graphene. *Nature Nanotech.*, 4, pp. 25–29, 2008.
- [55]. J. R. Lomeda, C. D. Doyle, D. V. Kosynkin, W. F. Hwang and J. M. Tour, Diazonium functionalization of surfactant-wrapped chemically converted graphene sheets, *J. Am. Chem. Soc.*, 130, pp. 16201–16206, 2008.
- [56]. S. Stankovich, D. A. Dikin, G. H. B. Dommett, K. M. Kohlhaas, E. J. Zimney, E. A. Stach, R. D. Piner, S. T. Nguyen and R. S. Ruoff, Graphene-based composite materials, *Nature*, 442, pp. 282–286, 2006.
- [57]. J. Li, C. Liu, Chao Cheng, Electrochemical detection of hydroquinone by graphene and Pt-graphene hybrid material synthesized through a microwave-assisted chemical reduction process, *Electrochimica Acta*, 56, pp. 2712-2716, 2011.
- [58]. Y. Si and E. T. Samulski, Synthesis of water soluble graphene, *Nano Lett.*, 8, pp. 1679–1682, 2008.

- [59]. D. W. Boukhvalov, and M. I. Katsnelson, Modeling of graphite oxide. *J. Am. Chem. Soc.*, 130, pp. 10697–10701, 2008.
- [60]. G. Wang, J. Yang, J. Park, X. Gou, B. Wang, H. Liu and J. Yao, Facile synthesis and characterization of graphene nanosheets, *J. Phys. Chem. C*, 112, pp. 8192–8195, 2008.
- [61]. H. C. Schniepp, J. L. Li, M. J. McAllister, H. Sai, M. Herrera-Alonso, D. H. Adamson, R. K. Prud'homme, R. Car, D. A. Saville and I. A. Aksay, Functionalized Single Graphene Sheets Derived from Splitting Graphite Oxide, *J. Phys. Chem. B*, 110, pp. 8535-8539, 2006.
- [62]. M. Jin, T. H. Kim, S. C. Lim, D. L. Duong, H. J. Shin, Y. W. Jo, H. K. Jeong, J. Chang, S. Xie, and Y. H. Lee, Facile Physical Route to Highly Crystalline Graphene, *Adv. Funct. Mater.*, 21, pp. 3496–3501, 2011
- [63]. Y. Zhu, S. Murali, M. D. Stoller, A. Velamakanni, R. D. Piner, R. S. Ruoff, Microwave assisted exfoliation and reduction of graphite oxide for ultracapacitors, *Carbon*, 48, pp. 2106–2122, 2010.
- [64]. M. F. El-Kady, V. Strong, S. Dubin, R. B. Kaner, Laser Scribing of High-Performance and Flexible Graphene-Based Electrochemical Capacitors, *Science*, 335, pp. 1326-1330, 2012.
- [65]. Y. Zhu, S. Murali, W. Cai, X. Li, J. W. Suk, J. R. Potts, R. S. Ruoff, Graphene and Graphene Oxide: Synthesis, Properties, and Applications, *Adv. Mater.*, 22, pp. 3906–3924, 2010.

- [66]. L. L. Zhang, R. Zhou and X. S. Zhao, Graphene-based materials as supercapacitor electrodes, *J. Mater. Chem.*, 20 , pp. 5983–5992, 2010.
- [67]. B. E. Conway, Transition from "supercapacitor" to "battery" behavior in electrochemical energy storage, *Journal of the Electrochemical Society*, 138, pp. 1539-1548, 1991.
- [68]. B.E. Conway, V. Birss, J. Wojtowicz, The role and utilization of pseudocapacitance for energy storage by supercapacitors, *J. Power Sources*, 66, pp. 1-14, 1997.
- [69]. M. E. Roberts, D. R. Wheeler, B. B. McKenzie and B. C. Bunkera, High specific capacitance conducting polymer supercapacitor electrodes based on poly(tris(thiophenylphenyl)amine), *J. Mater. Chem.*, 19, pp. 6977-6979, 2009.
- [70]. J. Yana, T. Weia, Z. Fana, W. Qian, M. Zhang, X. Shen, and F. Wei, Preparation of graphene nanosheet/carbon nanotube/polyaniline composite as electrode material for supercapacitors, *J. Power Sources*, 195, pp. 3041–3045, 2010.
- [71]. E. Frackowiaka, V. Khomenkob, K. Jurewicza, K. Lotaa, and F. B éguin, Supercapacitors based on conducting polymers/nanotubes composites, *J. Power Sources*, 153, 28, pp.413–418, 2006.
- [72]. C. D. Lokhandea, D. P. Dubal, and O. S. Joo, Metal oxide thin film based supercapacitors, *Current Applied Physics*, 11, pp. 255-270, 2011.
- [73]. J. P. Zheng, P. J. Cygan and T.R. Jow, Hydrous Ruthenium Oxide as an Electrode Material for Electrochemical Capacitors, *J. Electrochem. Soc.*, 142, pp. 2699-2703, 1995.

- [74]. A. Cornell and D. Simonsson, Ruthenium Dioxide as Cathode Material for Hydrogen Evolution in Hydroxide and Chlorate Solutions, *J. Electrochem. Soc.*, 140, pp. 3123-3129, 1993.
- [75]. B. E. Conway, *Electrochemical Supercapacitors: Scientific Fundamentals and Technological Applications*, Plenum Publishers, New York, NY, 1999.
- [76]. Y. Chen, X. Zhang, D. Zhang, P. Yu and Y. Ma, High performance supercapacitors based on reduced graphene oxide in aqueous and ionic liquid electrolytes, *Carbon*, 49, pp. 573–580, 2011.
- [77]. A. Balducci, R. Dugas, P.L. Taberna, P. Simon, D. Pl e, M. Mastragostino, S. Passerini, High temperature carbon–carbon supercapacitor using ionic liquid as electrolyte, *J. Power Sources*, 165, pp. 922–927, 2007.
- [78]. P. Delhaes, *Graphite and Precursors*, CRC Press, Boca Raton, FL, 2001.
- [79]. A. C. Ferrari, J. C. Meyer, V. Scardaci, C. Casiraghi, M. Lazzeri, F. Mauri, S. Piscanec, D. Jiang, K. S. Novoselov, S. Roth, and A. K. Geim, Raman Spectrum of Graphene and Graphene Layers, *Phys. Rev. Lett.*, 97, pp. 187401-187401-4, 2006.
- [80]. D. Yang, A. Velamakanni, G. Bozoklu, S. Park, M. Stoller, R. D. Piner, S. Stankovich, I. Jung, D. A. Field, C. A. Ventrice Jr., R. S. Ruoff, Chemical analysis of graphene oxide films after heat and chemical treatments by X-ray photoelectron and Micro-Raman spectroscopy, *Carbon*, 47, pp. 145-152, 2009.
- [81]. C. Kozlowski, P. M. A. Sherwood, X-ray photoelectron spectroscopic studies of carbon-fibre surfaces. Part 4. The effect of electrochemical treatment in nitric acid, *J. Chem. Soc., Faraday Trans. 1*, 80, pp. 2099-2107, 1984.

- [82]. A. Kaniyoor, T. T. Baby, S. Ramaprabhu, Graphene synthesis via hydrogen induced low temperature exfoliation of graphite oxide, *J. Mater. Chem.*, 20, pp. 8467-8469, 2010.
- [83]. W. Gao, L. B. Alemany, L. Ci and P. M. Ajayan, New insights into the structure and reduction of graphite oxide, *Nat. Chem.*, 1, pp. 403-408, 2009.
- [84]. G. Wang, X. Shen, J. Yao and J. Park, Graphene nanosheets for enhanced lithium storage in lithium ion batteries, *Carbon*, 47, pp. 2049-2053, 2009.
- [85]. S. Zhang, N. Sun, X. He, X. Lu, and X. Zhang, Physical Properties of Ionic Liquids: Database and Evaluation, *J. Phys. Chem. Ref. Data*, 35, pp. 1475-1517, 2006.
- [86]. X. Yang, C. Cheng, Y. Wang, L. Qiu, D. Li, Liquid-Mediated Dense Integration of Graphene Materials for Compact Capacitive Energy Storage, *Science*, 341, pp. 534-537, 2013

Appendix A: List of abbreviations

The following table includes the abbreviations and acronyms used throughout the thesis. The page where each acronym is defined or first used is given.

Acronym	Meaning	Page
GO	Graphite oxide	iii
HAG	Hydrogen annealed graphene	38
rGO	Reduced graphene oxide	iii
AC	Activated carbon	17
CNT	Carbon nanotube	17
PEM	Proton exchange membrane	8
EDL	Electric double-layer	ii
DMF	Dimethylformamide	27
NMP	N-methyl-2-pyrrolidone	27
THF	Tetrahydrofuran	27
AFM	Atomic force microscopy	27
PANI	Polyaniline	31
PPy	Polypyrrole	31
PEDOT	Poly-(3,4-ethylenedioxythiophene)	31
pTTPA	Poly(Tri(4-(Thiophen-2-yl)Phenyl)Amine)	31
PYR ₁₄ TFSI	N-butyl-N-methylpyrrolidinium bis(trifluoromethanesulfonyl)imide	33

PP	Polypropylene	34
SEM	Scanning electron microscopy	iii
FESEM	Field emission scanning electron microscopy	40
TEM	Transmission electron microscopy	iii
BET	Brunauer-Emmett-Teller	iii
BJH	Barrett-Joyner-Halenda	42
XRD	X-ray diffraction	iii
XPS	X-ray photoelectron spectroscopy	iii
FTIR	Fourier transform infrared spectroscopy	iii
CV	Cyclic voltammetry	iii
GCD	Galvanostatic charge-discharge	52
ESR	Equivalent series resistance	10